Record of tropical interannual variability of temperature and water vapor from a combined AIRS-MLS data set

C. K. Liang,[1,2] A. Eldering,[3] A. Gettelman,[4] B. Tian,[3] S. Wong,[3] E. J. Fetzer,[3] and K. N. Liou[1,2]

Received 29 July 2010; revised 15 December 2010; accepted 3 January 2011; published 23 March 2011.

[1] We utilize a merged AIRS and MLS temperature and water vapor record (August 2004 to March 2010) to study the atmospheric variability of these quantities. The seasonal and spatial distribution of temperature and humidity shows the tropical western Pacific (TWP, 8°S–8°N, 120°E–170°E) to be a location with persistent deep convection and the tropical central Pacific (TCP, 8°S–8°N, 120°W–170°W) to be a region of subsidence, consistent with previous work. Furthermore, our estimates of 3.9 ± 0.3 ppmv and 4.9 ± 0.9 ppmv for the tropical mean stratospheric entry water vapor concentration and saturation mixing ratio, respectively, are well within previous estimates from a wide variety of observations. We also find that the interannual variability modes of the El Niño–Southern Oscillation (ENSO) and the quasi-biennial oscillation (QBO) both impact the tropopause region. The TWP (TCP) experiences enhancements (cancellation) of temperature anomalies when the ENSO and QBO are in phase. When these interannual modes fall out of phase the additive behavior of the anomalies migrate to the TCP with the TWP experiencing weaker anomalies. In both cases a change in the water vapor distribution is also observed. Our results are consistent with previous results, showing that this migration of anomaly enhancement and cancellation is a result of the ENSO impact on the Walker Circulation and the period when this occurs relative to the phase of the QBO. Our findings suggest that when the ENSO and QBO are out of phase, the TCP water vapor distribution may have a substantial impact on the tropical zonal water vapor distribution.

Citation: Liang, C. K., A. Eldering, A. Gettelman, B. Tian, S. Wong, E. J. Fetzer, and K. N. Liou (2011), Record of tropical interannual variability of temperature and water vapor from a combined AIRS-MLS data set, *J. Geophys. Res.*, *116*, D06103, doi:10.1029/2010JD014841.

1. Introduction

[2] It has been known for sometime that air enters the stratosphere via the tropical tropopause [*Brewer*, 1949]. Although increases in tropospheric water vapor (H_2O) are expected in a warming climate, perturbations to its amount in the upper troposphere (UT) produces the largest radiative changes relative to other regions of the atmosphere [*Held and Soden*, 2000]. Lower stratospheric (LS) water vapor also can have a significant impact on climate. The recent reduction in LS water vapor (mean difference taken between 2001–2005 and 1996–2000) resulted in a radiative forcing of −0.098 W/m^2 which offset part of the +0.26 W/m^2 forcing from the increase in CO_2 from 1996–2005 [*Solomon et al.*, 2010]. Furthermore, changes to stratospheric water vapor may have consequences on future stratospheric ozone concentrations [*Kirk-Davidoff et al.*, 1999]. Changes in water vapor will also affect the frequency of cirrus occurrence, therefore, also impacting the radiative balance of the UTLS [e.g., *Gettelman et al.*, 2004; *Corti et al.*, 2005]. Thus, quantifying the processes that govern the distribution of UTLS water vapor is crucial.

[3] The upper tropospheric/lower stratospheric (UTLS) water vapor budget is largely determined by contributions from localized convective moistening [*Soden*, 2004; *Horváth and Soden*, 2007], dehydration [e.g., *Fueglistaler et al.*, 2005; *Fueglistaler and Haynes*, 2005], horizontal advection through cold trap regions, precipitating thin cirrus [*Holton and Gettelman*, 2001], and convective mixing [*Sherwood and Dessler*, 2001, 2003]. Furthermore, interannual variability modes such as the El-Niño–Southern Oscillation (ENSO) [*Philander*, 1990; *Wallace et al.*, 1998] and the quasi-biennial oscillation (QBO) [*Reed*, 1965b, 1965a; *Hamilton*, 1984; *Dunkerton*, 1985], also affect the UTLS temperature, and thus, water vapor distribution. *Gettelman et al.* [2001] showed that the ENSO modulates tropopause temperatures

[1]Joint Institute for Regional Earth System Science and Engineering, University of California, Los Angeles, California, USA.
[2]Department of Atmospheric and Oceanic Sciences, University of California, Los Angeles, California, USA.
[3]Jet Propulsion Laboratory, California Institute of Technology, Pasadena, California, USA.
[4]Atmospheric Chemistry Division, National Center for Atmospheric Research, Boulder, Colorado, USA.

0148-0227/11/2010JD014841

in the TCP, making them colder (warmer) during El Niño (La Niña) periods. *Zhou et al.* [2001b] showed the same results for the tropical cold point tropopause (CPT). The QBO manifests itself as descending temperature anomalies [*Andrews et al.*, 1987] in thermal wind balance with the descending westerly/easterly wind anomalies, which are a result of the interaction between the zonal mean wind and the upward propagating equatorial waves (from tropical convection) in the stratosphere [*Baldwin et al.*, 2001]. Work by *Fueglistaler et al.* [2005] and *Fueglistaler and Haynes* [2005] showed that UTLS water vapor concentrations can be reconstructed tracing a parcels history back to the coldest temperature it experiences–this is termed the Lagrangian Cold Point (LCP)–and that the interannual modes of the ENSO and QBO both impact the LCP.

[4] *Zhou et al.* [2004] showed that differences in the dehydration volume, DV (defined as the volume of the atmosphere that dropped below a reference temperature of 192 K), of the UTLS depended on the ENSO and QBO impacts on TTL temperatures. Specifically, they found that the phase of the ENSO was a strong determinant of the size of DV. La Niña periods were found to produce larger DV in the TTL than El Niño years. Their work focused on the El Niño of boreal winter, 1983, and the La Niña of boreal winter, 1985, which incidentally coincided with periods when the ENSO and QBO [*Zhou et al.*, 2004, Figure 7] were in phase, i.e., El Niño (positive temperature anomalies) and La Niña (negative temperature anomalies) corresponding to westerly (positive temperature anomalies) and easterly (negative temperature anomalies) QBO regimes, respectively.

[5] Although significant progress has been made in understanding the processes that govern the interannual variations of UTLS temperature and water vapor, quantifying the effects of the ENSO and QBO on these quantities has been difficult due to a lack of measurements that span the troposphere and stratosphere. Previous satellite data records had limits in their vertical sensitivity, resolution, and spatial extent. For example, the GOES Visible Infrared Spin Scan Radiometer (VISSR) Atmospheric Sounder (VAS) was only able to retrieve water vapor in a single column mean layer over a depth of a few hundred millibars within the UT and nowhere below [*Soden and Bretherton*, 1993]. The Halogen Occultation Experiment (HALOE) [*Russell et al.*, 1993] and the Microwave Limb Sounder (MLS) [*Waters et al.*, 1999] on the Upper Atmosphere Research Satellite (UARS) used limb measurements to provide global coverage of water vapor measurements primarily in the LS. Temperature and water vapor measurements that span the entire troposphere and stratosphere are limited to sparsely located in situ instruments, making it difficult to explore the interaction between the ENSO and QBO.

[6] We develop a tropical time record of water vapor, temperature, and relative humidity (RH), for pressures between 1013 hPa and 10 hPa, from a newly combined Atmospheric Infrared Sounder (AIRS) [*Aumann et al.*, 2003; *Susskind et al.*, 2006; *Divakarla et al.*, 2006; *Fetzer et al.*, 2008; *Chahine et al.*, 2006] and Microwave Limb Sounder (MLS) [*Waters et al.*, 2006; *Read et al.*, 2007] data set [*Liang et al.*, 2010] for the majority A-Train record (August 2004 to March 2010) when both instruments have colocated measurements (see section 2 for details). AIRS is able to retrieve temperature throughout the troposphere and stratosphere and water vapor from the surface up to around 261 hPa [e.g., *Liang et al.*, 2010], losing sensitivity for lower pressures. The MLS provides high-quality stratospheric and UT ($P \leq$ 316 hPa) water vapor retrievals but often becomes saturated at higher pressures. *Liang et al.* [2010] merged the AIRS and MLS water vapor profiles to create the first global satellite record of water vapor that spans the entire troposphere and stratosphere. We use these profiles to characterize the tropical distribution of temperature and water vapor.

[7] The evolution of water vapor, temperature, and RH over the entire data record (sections 3.2 and 3.4) is analyzed to investigate how the ENSO might impact the QBO temperature signals in the TTL and the subsequent effects on the tropopause region (around 100 hPa) water vapor distribution. Section 2 summarizes the data set and analysis method to construct the time record, section 3 summarizes the data analyses results of the temperature, water vapor, and RH time record, and concluding remarks are made in section 4.

2. Data and Methodology

2.1. A-Train Soundings

[8] The water vapor profiles are taken from two sources: (1) the AIRS [*Aumann et al.*, 2003] and (2) the MLS [*Waters et al.*, 2006], which fly on the Aqua and Aura spacecrafts, respectively. The AIRS, which flies on a Sun-synchronous orbit with equatorial crossing times of 1330 (ascending) and 0130 (descending) local time, uses a variety of spectra from infrared to microwave frequencies to retrieve water vapor in conditions with up to 70% cloud fraction. The Aura spacecraft lagged Aqua by about 14 minutes until the beginning of 2008, but due to the limb scanning geometry of MLS, its measurements only lagged those of AIRS by about 8 min. From 15 May 2008 the Aura spacecraft was maneuvered to colocate MLS and CloudSat measurements, which reduced the lag between AIRS and MLS measurements to about 1 min.

[9] AIRS can retrieve temperature from the surface up to regions in the stratosphere (~10 hPa) and water vapor for $P \geq 250$ hPa with nominal vertical resolutions of ~2–3 km for both parameters. MLS can retrieve water vapor from 0.1–316 hPa with a nominal vertical resolution of ~2 km. The joint AIRS/MLS water vapor profiles developed by *Liang et al.* [2010] and AIRS temperature profiles, for the period of August 2004 to March 2010, are used for this analysis. Briefly, *Liang et al.* [2010] analyzed the AIRS and MLS averaging kernels (AK) (these are functions that describe the vertical sensitivity of passive remote sensing instruments to atmospheric trace gases) and confirmed that the AIRS and MLS have overlapping sensitivity to UT water vapor around ~260 hPa; this was also shown through direct water vapor comparisons by *Read et al.* [2007] and *Fetzer et al.* [2008]. Both instruments have vertical resolutions that range between ~2 and 3 km. However, for pressures $P < 260$ hPa the AIRS sensitivity, diagnosed from the AK, drops dramatically while the MLS has strong sensitivity to water vapor throughout the TTL region. Therefore, for $P < 260$ hPa a weighted mean was constructed between the AIRS and MLS profiles using the AK as weighting factors. Because MLS saturates often and AIRS has high sensitivity to water vapor for $P \geq 260$ hPa the AIRS data was used for these pressures. The data domain for this work will be from 1013 hPa to 10 hPa. We do not account for the differences in the lag periods before and after

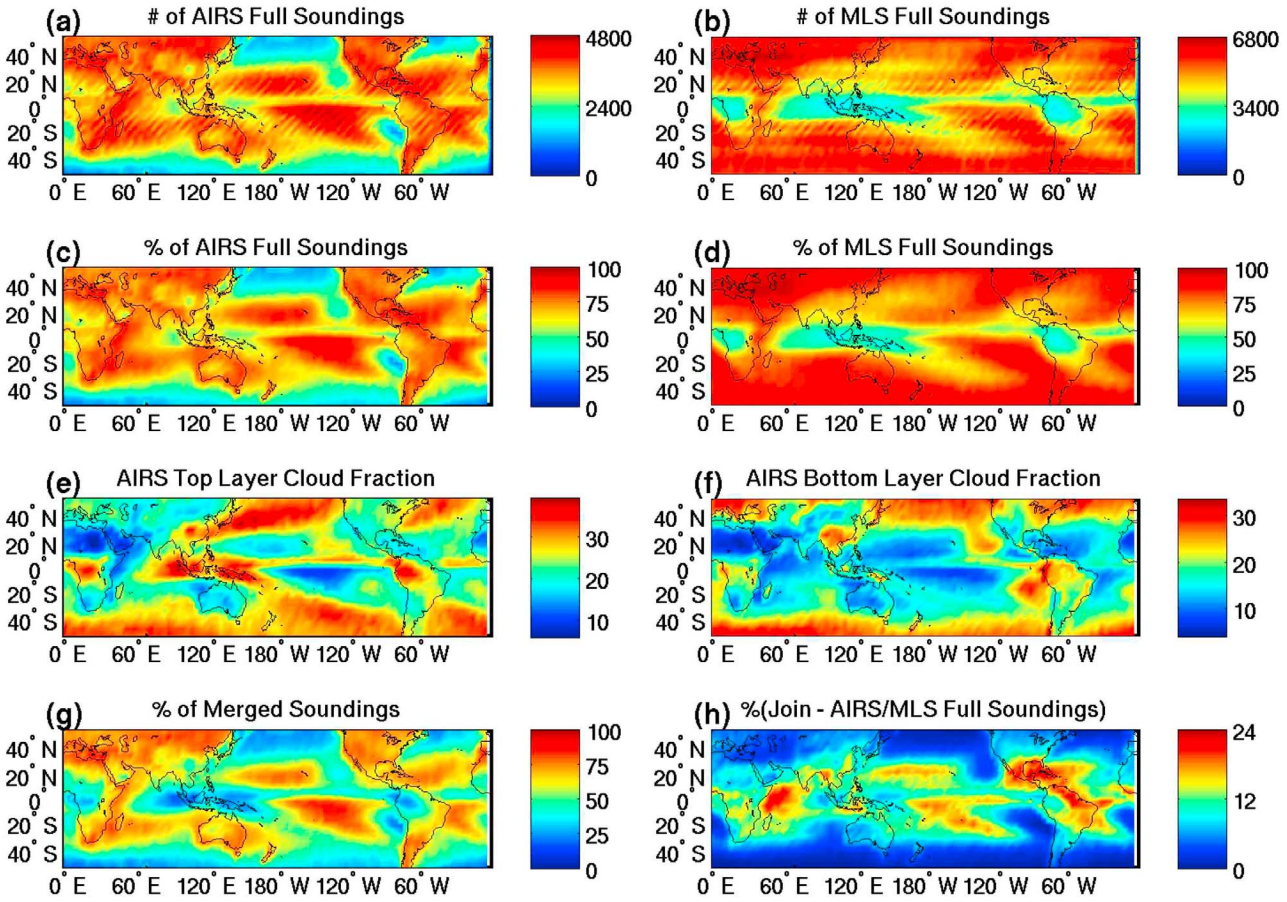

Figure 1. Statistics are for August 2004 to March 2010; they are gridded in 4° × 4° boxes, from 50°S–50°N. (a) Number of full AIRS temperature and water vapor soundings. (b) Number of full MLS water vapor soundings down to 316 hPa. (c and d) Same as Figures 1a and 1b but reported as a percentage of the total number of soundings. (e and f) The mean AIRS cloud fractions for the reported top and bottom retrieved cloud layers, (g) percent of grid boxes with usable merged profiles, and (h) the percentage difference between the number of full soundings between AIRS and MLS and the number of merged profiles (pixels for which AIRS has full soundings and MLS has profiles down to 215 hPa, rather than 316 hPa).

the 15 May 2008 spacecraft maneuver. We focus this analysis in the deep tropics between 8°S–8°N because it was found that the 100 hPa temperature signal associated with the QBO (for this data record) is strongest in this latitude band.

[10] In order to compute RH, the AIRS temperature profiles are used throughout the entire data domain per the recommendation of *Read et al.* [2007]. The saturation vapor pressure (e_s) over liquid and ice are computed using work by *Murphy and Koop* [2005]. The liquid and ice e_s are taken over temperature ranges of $T \geq 0$°C and $T \leq -20$°C, respectively. RH is just the ratio between the water vapor concentration and the saturation mixing ratio (q_s). For $-20 < T < 0$°C, RH is a linear interpolation between the values for ice and liquid.

[11] Quantifying the sampling of the data is necessary in order to identify any measurement biases. Figure 1 shows the joint sampling characteristic of AIRS and MLS. Figures 1a and 1b show the number of AIRS (water vapor and temperature) and MLS (water vapor) full soundings, respectively, for each 4° × 4° box over the latitude band of ~50°S–50°N. AIRS full soundings, in this study, are defined as profiles that have quality flags PGood = Psurf,i.e., profiles of PGood quality that reach the surface (see AIRS AMSU HSB Version 5 Level 2 Quality Control and Error Estimation, 2010, for quality flag details; http://disc.sci.gsfc.nasa.gov/AIRS/documentation/documentation.shtml). MLS full soundings are profiles (after a series of quality checks) with water vapor retrievals for pressures $P \leq 316$ hPa (see Version 2.2 level 2 data quality and description document, 2007, http://mls.jpl.nasa.gov/data/v2-2_data_quality_document.pdf) for quality flag details). Figures 1c and 1d report the values in Figures 1a and 1b, respectively, as a percentage of the total number of soundings (of any quality) in each grid box. One clear feature in Figure 1d is that the low sampling essentially follows the Intertropical Convergence Zone (ITCZ), a region with frequent deep convection. Although MLS can sound through optically thick clouds, the large ice hydrometeors in deep convective cloud tops cause enough scattering to impede the soundings. In Figure 1c one observes that AIRS also has sounding limitations in the tropics, primarily in regions of deep convection and persistent stratiform clouds. This is simply a limitation of the IR instrument since these stratiform clouds are usually optically thick enough to prevent any possible sounding through them. Furthermore, the AIRS cloud clearing algorithm requires

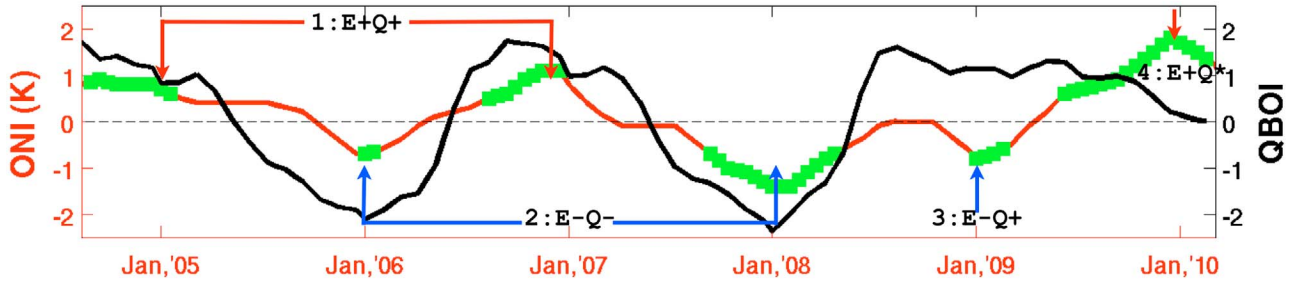

Figure 2. Time series of ONI (red) and QBOI (black). Green markers identify when SST anomalies exceed a magnitude of |0.5 *K*|. Specific ENSO composites are identified by 1:E+Q+, 2:E−Q−, 3:E−Q+, and 4:E+Q* (see text for details). The ENSO and QBO are in phase from the beginning of the time record until approximately boreal spring of 2008. Beyond this time the ENSO and QBO fall out of phase until the end of the record.

some clear sky in its field-of-view in order to estimate the clear versus cloudy radiances [*Susskind et al.*, 2006]. Stratiform clouds regularly have cloud fractions on the order of 80–100%,preventing AIRS from obtaining any useful information from the clear-sky radiances. Figures 1e and 1f show the annual mean cloud fractions reported by AIRS for its top and bottom cloud top pressures (CTP) (AIRS can report CTP for up to 2 cloud layers). One can see that regions of high (low) cloud fraction almost exactly overlay the regions of low (high) sampling in Figure 1c. Most of the clouds in Figure 1e are ice clouds with a peak in the CTP distribution around 200 hPa (not shown), while the clouds in Figure 1f primarily consist of water clouds with a peak in the CTP distribution around 650 hPa (not shown).

[12] From Figures 1a and 1c one might gather that AIRS can provide a high yield of tropical soundings of water vapor. However, *Liang et al.* [2010] showed that AIRS loses sensitivity to water vapor at levels above the 250–260 hPa layer in the 40°S–40°N latitude band. Using just the MLS profiles for pressures as high as 316 hPa would lead to the sampling in Figure 1d. However, combining the AIRS and MLS profiles as described by *Liang et al.* [2010], which uses AIRS from 1013–261 hPa and merges the AIRS and MLS water vapor profiles from 215 hPa to the top of atmosphere, results in the sampling shown in Figure 1g. Figure 1h shows the difference between using AIRS and MLS individually, i.e., the union of Figures 1c and 1d, versus the merged data set. One finds that the sampling increases by as much as 30% in the tropics when merging the profiles.

[13] It is noted that because both instruments have lower sampling in the tropics (due to high cloud cover), the subsequent water vapor climatologies are "dry biased" toward clear sky conditions. Nevertheless, as will be shown in section 3.4.5, the temperature (AIRS) and water vapor (AIRS and MLS) profiles still capture the latent heating and free tropospheric moistening associated with deep convection. Also, although the sampling is still biased toward lower cloud fractions, there are still over ~10^6 equatorial soundings, in clear and cloudy conditions, that provide enough information to discern the interannual variability of temperature and water vapor due to the ENSO and QBO.

[14] From the combined atmospheric profiles, an equatorial (8°S–8°N and 180°W–180°E) record of water vapor, temperature, and RH, from 1013 hPa to 10 hPa, is derived. The record is averaged in ~16 day bins (15 days for January, 16 days for January–December, and 14 (15) days for December in a 365 (366) day year) following the A-Train repeat cycle, i.e., the number of days it takes the A-Train satellites to repeat a particular orbital track. This helps to enhance the sampling size and minimize bias caused by missing data. The spatial distribution of the interannual signals is computed to identify the regions where the ENSO and QBO impact the tropopause region.

2.2. Ocean Niño Indices

[15] Although the data record is short, there are six ENSO events between August 2004 and March 2010. The ENSO events, identified by the Ocean Niño Indices (ONI) (NWS CPC, Ocean Niño Indices: ENSO cold and warm episodes by season, 2010, http://www.cpc.noaa.gov/products/analysis_monitoring/ensostuff/ensoyears.shtml), are shown in Figure 2. The ONI quantify the interannual sea surface temperature anomalies (SSTA) in the TCP (Niño3.4 region), with positive and negative SSTA associated with El Niño and La Niña. Each ONI comes from a running mean of SSTA over three consecutive months (e.g., December, January, February (DJF); January, February, March (JFM)). Periods with 3 month means exceeding |0.5 *K*| indicate significant ENSO events (green markers in Figure 2). Figure 2 also show the relevant ENSO composites for this study. Briefly, the 1:E+Q+ composite includes the two El Niño events surrounding DJF of 2005 and 2007, when the ENSO and QBO (westerly) are both in phase. The 2:E−Q− composite include the two La Niña events surrounding DJF of 2006 and 2008, when the ENSO and QBO (easterly) are in phase. The 3:E−Q+ and 4:E+Q* represent single seasonal composites of the 2009 La Niña and 2010 El Niño events which serve to highlight periods when the ENSO and QBO are out of phase (technically 4:E+Q* corresponds to an easterly transition of the QBO, pulling the QBO out of phase of El Niño).

2.3. Quasi-Biennial Oscillation Indices

[16] Figure 2 also shows the Quasi-Biennial Oscillation Indices (QBOI), which are derived from the 50 hPa zonal wind anomalies (zonally averaged over the equator; indices come from the National Centers for the Environmental Prediction (NCEP)/National Center for Atmospheric Research (NCAR) Climate Data Assimilation System (CDAS)). These are used to diagnose the amplitude and phase of the QBO because: (1) the onset of the QBO is near 50 hPa typically

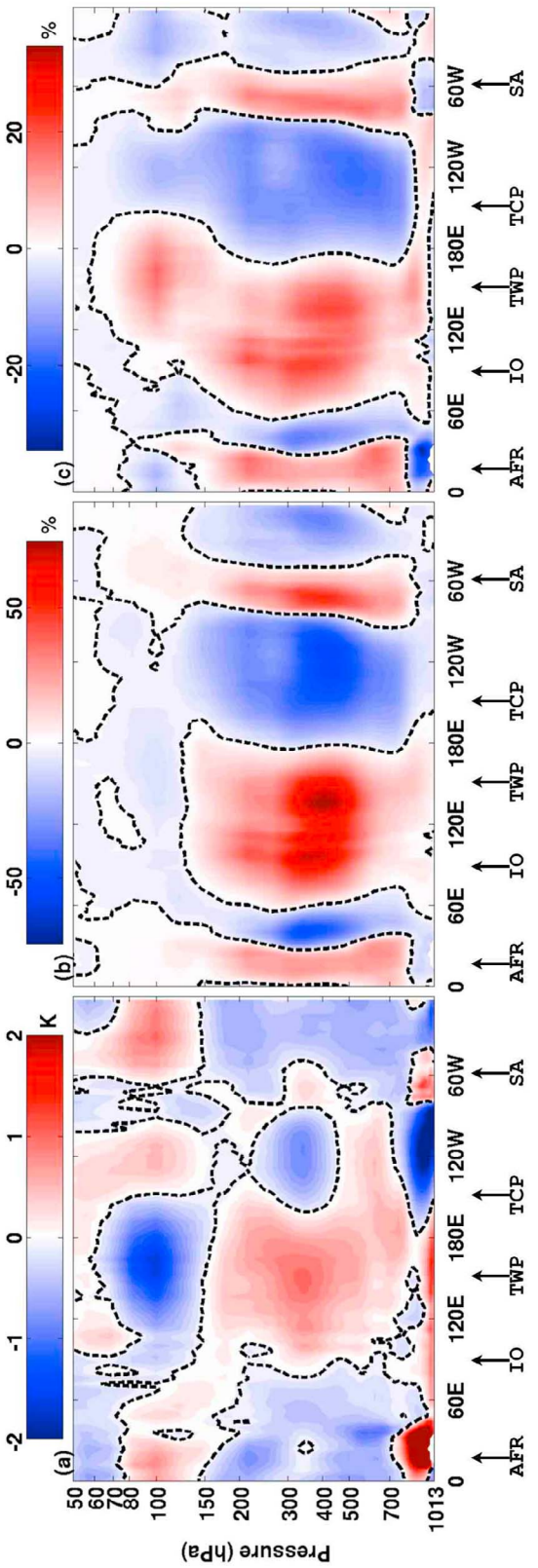

Figure 3. Temporal (from August 2004 to March 2010) and meridional (08°S–08°N) mean, pressure-longitude (4° longitude bins) cross sections of (a) temperature (K), (b) water vapor (reported as a % departure from the record mean water vapor concentration at each pressure level for each 4° longitude bin), and (c) relative humidity (%). Locations of the Indian Ocean (IO), tropical western Pacific (TWP), tropical central Pacific (TCP), Africa (AFR), and South America (SA) are identified.

around boreal spring, with maximum amplitudes around boreal winter [*Baldwin et al.*, 2001] and (2) the 50 hPa wind anomalies are best correlated with tropopause temperatures since the zonal wind shear at this level is in thermal wind balance with temperature anomalies in the lowest parts of the stratosphere [*Randel et al.*, 2000]. Positive and negative indices correspond to westerly and easterly wind anomalies. A full QBO period consists of a stratospheric westerly and easterly anomaly pair corresponding to positive and negative temperature anomalies. There are approximately two full QBO periods within the A-Train record, with periods of ~24 and ~30 months from boreal spring of 2005 to boreal spring of 2007, and the boreal spring of 2007 to boreal winter of 2010, respectively. We briefly note that *Huesman and Hitchman* [2001] use the 50–70 hPa wind shear as a QBO index rather than just the 50 hPa zonal winds; however, the choice of index does not impact our work as we produce similar results to theirs.

3. Results

3.1. Time Record Mean

[17] In this section, the basic tropical structure of temperature and water vapor is quantified. The time record means, taken from 8°S–8°N in longitude bins of 4°, are computed for temperature (Figure 3a), water vapor (Figure 3b), and relative humidity (Figure 3c) with the time record zonal mean removed at each pressure level and longitude bin. Temperature is reported as an absolute deviation from the time record zonal mean in Kelvin. Relative humidity is treated in the same manner but reported in percent (%). In order to show the water vapor structure through the entire vertical domain (1013 hPa to 10 hPa), the anomalies are computed as relative percent (%) deviations from the time record mean for each pressure level and longitude bin.

[18] The quadrupole structure in temperature (Figure 3a), from ~60–400 hPa and 100°E–60°W, reveals the typical dipole behavior of convection in the TWP and Indian Ocean (labeled as IO in Figure 3) and subsidence in the Niño3.4 region (herein referred as the TCP). *Fueglistaler et al.* [2009] confirmed a similar temperature structure with the European Centre for Medium-Range Weather Forecasts (ECMWF) reanalyses (their Figure 6a). The region between 150 and 70 hPa (TTL as defined by *Fueglistaler et al.* [2009]), reveals strong cold (warm) anomalies above the free-tropospheric heating (cooling) in the TWP (TCP). As in previous studies [e.g., *Holloway and Neelin*, 2007; *Sherwood and Dessler*, 2001], this is the expected behavior that results from tropical convection, although these studies (and perhaps others) ascribe this temperature pattern to different aspects of convection. A peculiar warm anomaly feature resides between 500 and 700 hPa and ~75°W–180°W, most likely due the latent heating of deep convective clouds, north of the equator, that persist throughout the year. Referring back to Figures 1e and 1f one finds, along the equator from the TCP to South America, a thin band of high cloud fractions. This corresponds to the AIRS CTP distribution peak between 600 and 700 hPa directly within the warm anomaly region over the TCP (not shown). The thin warm layer extends to the dateline then expands to the large warm anomalies seen throughout the free troposphere. The AIRS top layer cloud fractions in Figure 1e (top layer cloud distribution peaks around 200 hPa) show this

Table 1. Seasonal and Annual Mean Values of H_2O ($\overline{q}_v$), Temperature ($\overline{T}$), Saturation Mixing Ratio ($\overline{q}_s$), and Relative Humidity ($\overline{RH}$) at the Profile Cold Point[a]

	Season																	
	DJF (292,957; 47,205; 31,074)				MAM (267,804; 43,331; 30,974)				JJA (292,271; 47,831; 34,934)				SON (313,974; 52,341; 38,296)				Annual (1,167,006; 190,708; 135,278)			
Region	$\overline{q}_v$	$\overline{T}$	$\overline{q}_s$	$\overline{RH}$	$\overline{q}_v$	$\overline{T}$	$\overline{q}_s$	$\overline{RH}$	$\overline{q}_v$	$\overline{T}$	$\overline{q}_s$	$\overline{RH}$	$\overline{q}_v$	$\overline{T}$	$\overline{q}_s$	$\overline{RH}$	$\overline{q}_v$	$\overline{T}$	$\overline{q}_s$	$\overline{RH}$
Trop.	3.2 ± 0.3	189.5	3.3 ± 0.6	108 ± 20	3.3 ± 0.3	190.0	3.5 ± 0.6	102 ± 19	4.4 ± 0.3	194.2	7.1 ± 1.2	67 ± 12	4.5 ± 0.4	192.5	5.5 ± 1.0	90 ± 16	3.9 ± 0.3	191.6	4.9 ± 0.9	91 ± 17
TCP	3.2 ± 0.3	189.7	3.4 ± 0.6	105 ± 20	3.3 ± 0.3	190.5	3.8 ± 0.7	92 ± 17	4.3 ± 0.3	193.6	6.3 ± 1.1	72 ± 13	4.3 ± 0.3	192.2	5.2 ± 0.9	91 ± 17	3.8 ± 0.3	191.5	4.7 ± 0.8	90 ± 17
TWP	2.9 ± 0.2	187.6	2.3 ± 0.4	132 ± 25	3.2 ± 0.3	188.8	2.8 ± 0.5	118 ± 22	4.2 ± 0.3	192.7	5.5 ± 1.0	82 ± 15	4.2 ± 0.3	191.1	4.4 ± 0.8	107 ± 20	3.7 ± 0.3	190.2	3.8 ± 0.7	109 ± 20

[a]Note that cold point temperatures were at 96 hPa 99% of the time. These are computed for the equatorial tropics (08°S–08°N,180°E–180°W), TWP (08°S–08°N, 120°E–170°E), and TCP (08°S–08°N,120°W–170°W). $\overline{q}_v$, $\overline{T}$, $\overline{q}_s$, and $\overline{RH}$ are in units of ppmv, K, ppmv, and %, respectively. Seasons: DJF, December–February; MAM, March–May; JJA, June–August; SON, September–November. Parenthetical values below seasons are the number of profiles that went into the calculation for (Tropical, TCP, TWP) data for each season. The $\overline{q}_v$ error estimates come from the MLS accuracy of 8% at 100 hPa. A temperature accuracy of ±1 K [*Tobin et al.*, 2006] is assumed for all $\overline{q}_s$ and $\overline{RH}$ values.

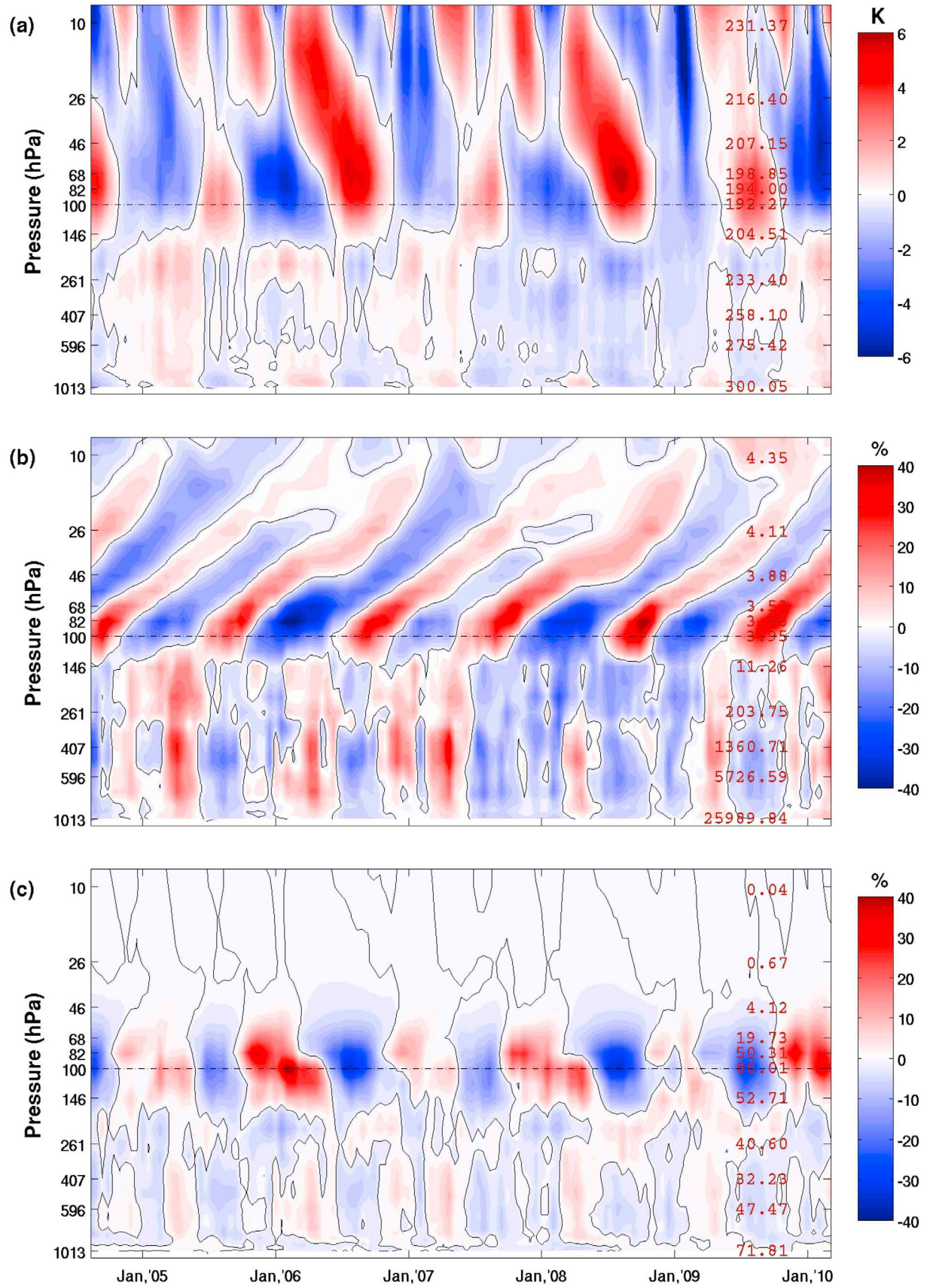
(a)
Pressure (hPa)
10
26
46
68
82
100
146
261
407
596
1013
231.37
216.40
207.15
198.85
194.00
192.27
204.51
233.40
258.10
275.42
300.05
K
6
4
2
0
-2
-4
-6
(b)
Pressure (hPa)
4.35
4.11
3.88
3.95
11.26
203.75
1360.71
5726.59
25989.84
%
40
30
20
10
0
-10
-20
-30
-40
(c)
Pressure (hPa)
0.04
0.67
4.12
19.73
50.31
52.71
40.60
32.23
47.47
71.81
%
40
30
20
10
0
-10
-20
-30
-40
Jan,'05
Jan,'06
Jan,'07
Jan,'08
Jan,'09
Jan,'10

Figure 4

transition between the TCP and TWP, revealing a zonal climatological signature of a transition from shallow convection to deep convection.

[19] Over the land masses of central Africa (labeled as AFR in Figure 3, 0°–40°E) and northern South America (labeled as SA in Figure 3, centered around 60°W), there are particularly large warm anomalies due to land surface warming; the anomalies over central Africa are on the order of ~10 K. The free troposphere above the land masses is cold even though deep convection frequents these areas [*Mitchell and Wallace*, 1992]. Since the temperature anomalies are calculated as deviations from the zonal mean, the cold anomalies from ~70°W–70°E are likely due to the TWP and Indian Ocean having a much warmer free troposphere than the rest of the tropics.

[20] The water vapor time record mean (Figure 3b) shows a dipole structure between the TWP/Indian Ocean (moister, convective) and TCP (drier, subsidence) regions from the surface up to the lower half of the TTL. Local extrema of moist (dry) anomalies, centered around 450 hPa, exist over the TWP (TCP). The moist features over central Africa in Figure 3 and South America are probably due to the moistening of deep convection, but the near surface anomalies are drier since they are over land masses. Although cold anomalies exist over these land masses in the free troposphere, evaporative moistening seems to dominate these regions. One other feature to note is the slight positive water vapor anomalies of 2–9%, i.e., 0.1–1 ppmv, from 70 to 150 hPa over these land regions.

[21] In Figure 3c, the TTL RH distribution is tightly coupled to TTL temperatures due to the exponential dependence of q_s on temperature and the aridity of the stratosphere. RH, in the UT and down throughout the free troposphere and boundary layer, however, correlates more strongly with water vapor. Also, in the TWP there is a thin layer near the surface of slightly negative RH anomalies due to the slightly stronger temperature anomalies at the surface. Slightly positive RH anomalies are observed in the TCP in the boundary layer, near 120°W, due to colder than average boundary layer temperatures. The positive RH in the TWP TTL results from the TWP having the coldest temperatures in the deep tropics leading to persistent saturation/supersaturation most of the year (see Table 1).

3.2. Time Evolution of Temperature, Water Vapor, and RH

[22] Figure 4 shows the zonal mean time evolution, between 8°S and 8°N, of temperature (Figure 4a), water vapor (Figure 4b), and RH (Figure 4c). Each time series represents ~16 day means (see section 2 for details) reported as anomalies from the time record zonal mean at each pressure level. The temperature anomalies range between ±6 K, with the largest anomalies above the tropopause region. The lapse rate $-\delta T/\delta z$ (not shown), between the surface and ~300 hPa, varies between 4 and 8 K/km, where the temperature roughly follows a moist adiabat in the tropical mean; the lapse rate between 125 and 300 hPa approaches a dry adiabat with values around 8 K/km. The time record shows predominately warm free tropospheric temperatures, consistent with the results of Figure 3a, with interannual impacts evident in 2006 (cold temperatures the whole year). The tropical mean 100 hPa temperature is ~192 K, consistent with values derived from reanalyses by *Randel et al.* [2000] and rawinsondes from *Zhou et al.* [2001a]. *Tobin et al.* [2006] showed that the mean AIRS bias between the surface and 100 hPa only ranged between ±1 K with the largest magnitudes occurring at 100 hPa. However, comparisons of AIRS and Constellation Observing System for Meteorology Ionosphere and Climate (COSMIC) soundings (boreal summer and fall) show the AIRS systematic error for 100 hPa temperatures is closer to ±~0.5K (S. Wong, JPL/Caltech, personal communication, 2010). This indicates that the observed temperature signal throughout the atmosphere is greater than the measurement accuracy which gives us confidence in the observed temperature features.

[23] Transitioning to Figure 4b, the well-known ascending water vapor tape recorder [*Mote et al.*, 1996, and references therein] is observed with anomalies reaching ±~40% of 3.9 ± 0.3 ppmv. The time-averaged water vapor mixing ratio (3.9 ppmv) is consistent with the values of the stratospheric entry level water vapor concentrations listed in Table 1 of *Zhou et al.* [2001a]. The stated MLS accuracy at 100 hPa is ~8% [*Read et al.*, 2007], so the observed water vapor anomalies are well outside the measurement uncertainty. The water vapor mixing ratios increase with altitude in the stratosphere due to methane oxidation (not shown). The 100 hPa water vapor data presented here are a weighted mean between AIRS and MLS water vapor. However, since the 100 hPa water vapor values are heavily weighted by MLS, due to AIRS virtually having no sensitivity at this level, the MLS accuracy estimate still holds (this holds for $P <$ 100 hPa as well) [*Liang et al.*, 2010]. There are time periods when the tropospheric moist (dry) anomalies share the same sign as the moist (dry) anomalies associated with the water vapor tape recorder (e.g., see moist anomalies directly after January, 2007 and dry anomalies in the latter half of 2007 in Figure 4b). Within the water vapor series, aspects of the tropospheric interannual signal of water vapor, for example, large areas of negative anomalies (blue) starting in the second half of 2007 and ending around the first half of 2009, are also discernible. In the time mean, the free troposphere is predominately moist, most likely due to the strong convection in the TWP, South America, and Africa (see Figure 3b). Interannual variations are also observed in the stratospheric water vapor tape recorder [*Randel et al.*, 1998; *Geller et al.*, 2002].

[24] The mean tropical surface layer RH (Figure 4c) is ~70% (shown at the bottom right ordinate) and drops off rapidly throughout the free troposphere, though it is still primarily moist (See Figure 3c). RH rises again in the TTL up

Figure 4. Equatorial mean (08°S–08°N, 180°E–180°W) time evolution of (a) temperature (K), (b) water vapor (%), and (c) RH (%) with the time record mean removed at each pressure level. Data spans between August 2004 and March 2010. Abscissa is time and ordinate is pressure. The black dash-dotted horizonal line denotes the 100 hPa level. Red text at the right ordinate is the time record mean for the specified pressure levels at the left ordinate. Herein all contour time record plots of pressure versus time will contain these mean values.

to the tropopause due to the strong temperature effect on q_s with very low water vapor concentrations. A reduction of RH once again occurs in the stratosphere due to the aridity of the stratosphere and the increase of temperature due to ozone absorption (not shown).

3.3. Cold Point Seasonal Cycle

[25] The scientific literature indicates that the tropical mean water vapor amount that enters the stratosphere is ~3.8 ppmv with a mean q_s of ~4.5 ppmv [e.g., *Zhou et al.*, 2001a; *Fueglistaler et al.*, 2009]. Table 1 summarizes the seasonal and annual means of q_v, q_s, and RH for the equatorial tropics (Trop), TCP, and TWP. Previous studies [e.g., *Mote et al.*, 1996] have indicated that to determine the correct q_s and stratospheric entry amount of water vapor, one needs to compute these quantities at the coldest temperatures in each profile. AIRS temperature profiles show that the cold point lies at 96 hPa (99% of the time), slightly higher in pressure than previous cold point pressure estimates of ~90 hPa [e.g., *Fueglistaler et al.*, 2009]. Since AIRS has coarser resolution in the UTLS (~3 km) it is not surprising that the observed cold point occurs at a higher pressure. It is noted that *Dessler* [1998] and *Zhou et al.* [2001a] estimated the stratospheric entry water vapor concentration from the minimum of q_s rather than the minimum temperature derivation of q_s. Both methods were exercised for this work and the results of Table 1 do not change within the AIRS temperature uncertainty estimates.

[26] The seasonal means show very clear seasonal cycles over all regions with boreal winter and spring corresponding to the driest and coldest seasons. The tropical annual mean q_s ($\overline{q}_s$) of 4.9 ± 0.9 ppmv is well within the estimates of the values listed in Table 1 of *Zhou et al.* [2001a]. This estimate for $\overline{q}_s$ is also consistent with the estimate from *Dessler* [1998]. The relatively large uncertainty on $\overline{q}_s$ is due to using a more conservative systematic temperature error estimate of 1 K [*Tobin et al.*, 2006]. However, assuming a systematic error of ~|0.5| K (from the AIRS and COSMIC comparison) essentially reduces all error bars in $\overline{q}_s$ and $\overline{RH}$ by about a factor of 2. The tropical annual mean water vapor concentration at the cold point ($\overline{q}_v$) of 3.8 ± 0.3 ppmv is well within the estimates in Table 1 of *Zhou et al.* [2001a]. Note that we do not account for midlatitude sources of water vapor that can contribute to tropical stratospheric water vapor concentrations [*Dessler*, 1998]. Therefore, our estimate of the entry level water vapor concentration will be high. The TWP is supersaturated (with respect to ice) almost year around due to this area having the coldest tropical temperatures. The results in Table 1 verify the seasonal and annual means are consistent with previous studies, giving us confidence in the AIRS and MLS data.

3.4. Interannual Variability

[27] Sections 3.2 and 3.3 showed that AIRS and MLS do capture the expected behavior of temperature and humidity within the instrumental uncertainty. Interannual variations were also identified in the data record. The two primary interannual modes that modulate tropical temperatures and water vapor are the ENSO and QBO, thus the remainder of this work will focus on these two modes of tropical variability. Note that for the rest of this work the 100 hPa temperatures will be used as a cold point proxy to study the effects of the ENSO and QBO on the temperature and water vapor distribution around the tropopause.

3.4.1. Zonal Equatorial Mean Interannual Time Series

[28] To remove the record mean annual cycle, the mean is computed (for temperature, water vapor, and RH) over all years in bins of ~16 days (see section 2 for details on bin construction). This is then subtracted from the same 16 day bins for each year; equation (1) illustrates this more clearly. The interannual signal for parameter "X" is calculated in the following manner:

$$\Delta X_i^j = X_i^j - \sum_j X_i^j \tag{1}$$

for the ith time record bin (~16 days/bin) within the jth year. ΔT and ΔRH, the interannual signals for temperature and RH, are computed using the above equation. Δq, the interannual signal for water vapor, is expressed as a percent deviation from the record mean annual cycle by dividing Equation (1) by $\Sigma_j X_i^j$; Figure 5 shows these quantities.

[29] Figure 5a shows the tropopause region ΔT has peak-to-peak amplitudes (~1.5 K) that are about half the observed maximum tropopause region peak-to-peak temperature anomalies (~4 K) presented in Figure 4a. Boundary layer and free tropospheric ΔT follow the ONI with warm (red colors in Figure 5a) and cold (blue colors in Figure 5a) periods corresponding to El Niño and La Niña events, respectively, highlighting the dominance of ENSO on the zonal mean temperature structure. In some periods, e.g., around January 2007 during an El Niño, ΔT in the UTLS (~150–70 hPa) has the same sign as the free tropospheric ΔT, while other periods, for example, boreal winter of 2009 during a La Niña, the free tropospheric and UTLS ΔT have opposite signs. This is because the zonal mean anomalies in the LS down to 100 hPa is mainly determined by the downward phase propagation of the QBO, while the anomalies in the free troposphere and the UT are primarily controlled by ENSO which does not have a regular cycle like the QBO.

[30] The Δq signal (Figure 5b) is about half (~0.5 ppmv) the water vapor anomalies (~1.2 ppmv) shown in Figure 4b for the peak-to-peak amplitudes. The vertically propagating signal (in time), starting around 100 hPa (denoted by the black dashed line), represents the interannual variability of the water vapor tape recorder [*Randel et al.*, 1998; *Geller et al.*, 2002]. The zonal mean Δq is also dominated by the ENSO through the free troposphere, and up to the bottom of the TTL, with moist (red) and dry (blue) regions corresponding to El Niño and La Niña events. This indicates the influence of the lower tropospheric processes on the UTLS water vapor distribution that is associated with ENSO events. Once again, there are periods (see DJF of 2005, 2006, 2007, and 2008) when the prevailing free tropospheric Δq share the same sign as those in the UTLS. This is a result of the joint impact of the ENSO and QBO being in phase and simultaneously dehydrating TTL air more (less) effectively during La Niña (El Niño) years [*Zhou et al.*, 2004]. This simultaneous ENSO and QBO impact will be discussed in more detail below. ΔRH (Figure 5c) in the ULTS almost exactly mimics ΔT with the largest anomalies in the TTL. However, moving further down into the free troposphere ΔRH signal is reduced from UTLS values and does not correlate well with the ONI or QBOI. This is consistent with RH remaining

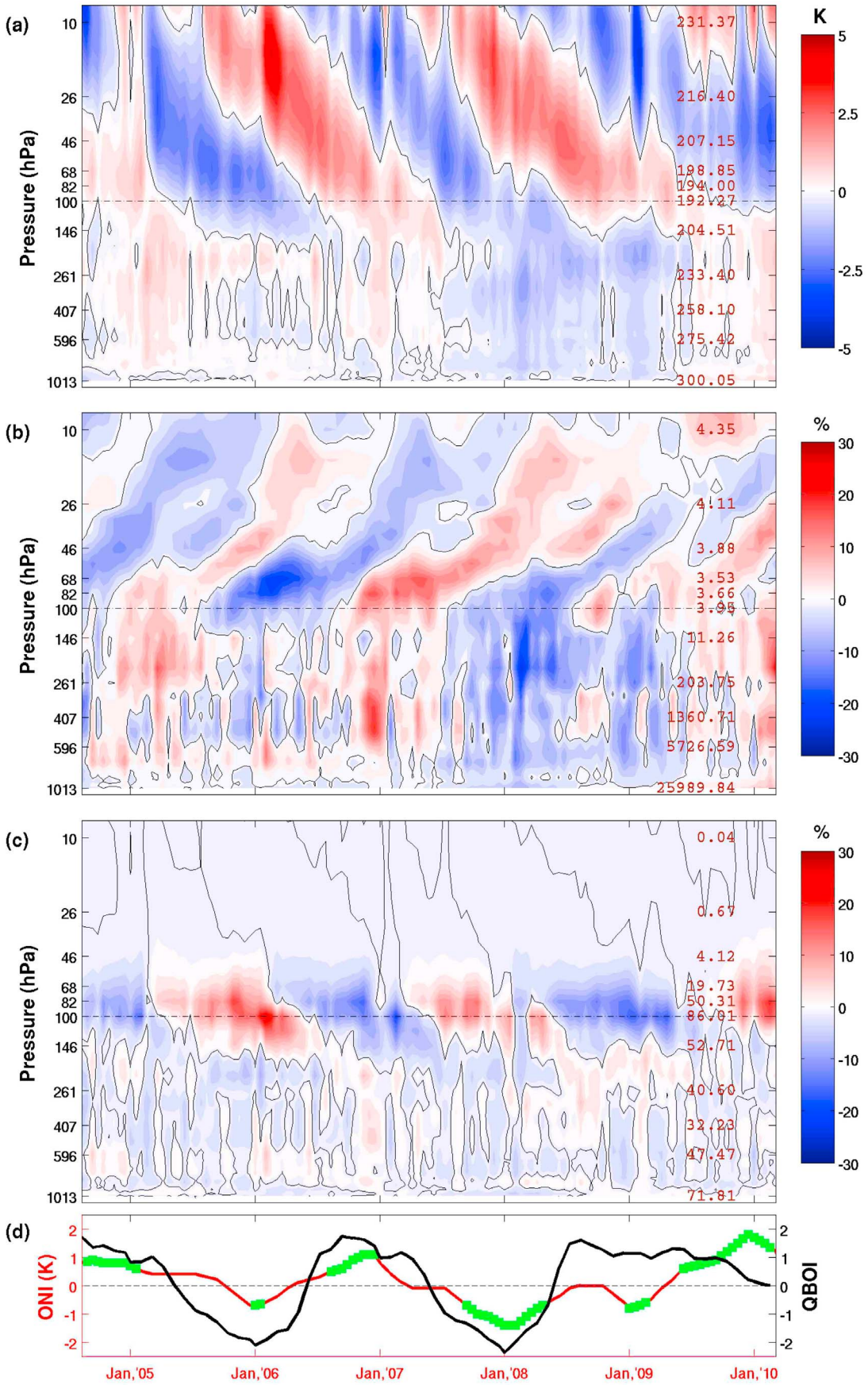
(a)
Pressure (hPa)
10
26
46
68
82
100
146
261
407
596
1013
231.37
216.40
207.15
198.85
194.00
192.27
204.51
233.40
258.10
275.42
300.05
K
5
2.5
0
-2.5
-5
(b)
Pressure (hPa)
4.35
4.11
3.88
3.53
3.66
11.26
203.75
1360.71
5726.59
25989.84
%
30
20
10
0
-10
-20
-30
(c)
Pressure (hPa)
0.04
0.67
4.12
19.73
50.31
86.01
52.71
40.60
32.23
47.47
71.81
%
30
20
10
0
-10
-20
-30
(d)
ONI (K)
2
1
0
-1
-2
QBOI
Jan,'05
Jan,'06
Jan,'07
Jan,'08
Jan,'09
Jan,'10

Figure 5

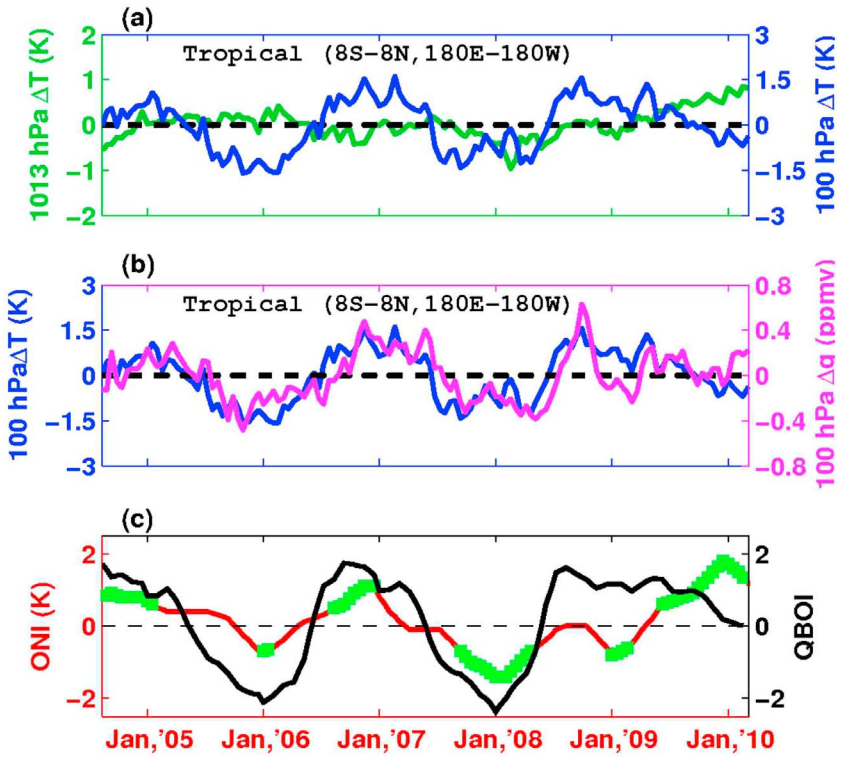

Figure 6. Equatorial mean (180°E–180°W, 08°S–08°N) interannual variability of (a) temperature at 1013 hPa (green) and 100 hPa (blue) and (b) temperature (blue) and water vapor (pink) at 100 hPa. (c) ONI and QBOI are plotted for reference.

constant with global changes to temperature and water vapor [e.g., *Soden et al.*, 2005].

[31] Shown in Figure 6a are the 1013 hPa (green) and 100 hPa (blue) ΔT for the entire equatorial region. The 100 hPa time record shows the cross section of anomalies denoted by the black dash-dotted lines in Figure 5. ENSO events alone should produce an anticorrelation between the 1013 hPa and 100 hPa ΔT since warmer (colder) SST should lead to stronger (weaker) convection which would lead to colder (warmer) tropopause temperatures [e.g., *Gettelman et al.*, 2001].There seems to be some anticorrelation in certain periods of ΔT between 1013 hPa and 100 hPa, however, computing a lag correlation over the entire time record results in a low correlation coefficient (R) of −0.13. This value is not surprising as: (1) our data includes land (land surface temperatures do not follow the ONI), (2) oceanic boundary layer ΔT are largely governed by the ENSO, and (3) 100 hPa ΔT are primarily governed by the QBO.

[32] Therefore, one might expect the 100 hPa ΔT to follow the QBOI rather than the ONI. A correlation coefficient of R = 0.86 (for lag 0) results from correlating the QBOI with 100 hPa ΔT with a confidence interval beyond 95%, reaffirming the thermal wind balance between 50 hPa and the lower stratosphere. The descending QBO ΔT is a minimum around 100 hPa, consistent with previous observations of the QBO [e.g., *Wallace*, 1973]. The 100 hPa anomalies are about 50% greater than those at 1013 hPa. This tropospheric amplification is consistent with work by *Santer et al.* [2005] and *Gettelman and Fu* [2008] where they find that UT temperature anomalies are amplified by a factor of ~1.5 from the surface.

[33] Figure 6b shows the same 100 hPa ΔT along with 100 hPa Δq (pink). Δq follows ΔT closely though with a lag of about a half a month. The lag correlation between ΔT and Δq yields R = 0.74 for lag +1 (~16 days) (at lag 0 R = 0.71). The lag correlation between Δq and the QBOI gives R = 0.74 (at lag +4) for lag of about 2.0 months (R = 0.60 for lag 0). The cause of the difference in lag correlation between ΔT and Δq and the QBOI and Δq is unknown. The low correlation between Δq and the ONI of R = 0.50 (lag 0) affirms that the 100 hPa ΔT is predominately determined by the QBO. At 121 hPa, the correlation between ΔT and Δq yields R = 0.78 for lag 0, suggesting the ~0.5 month lag at 100 hPa is likely a manifestation of MLS averaging ("smearing") features of the water vapor tape recorder from higher altitudes; MLS has a nominal vertical resolution of 2 km which may not be able to resolve the details of the cold point tropopause (although other transport processes may play a role in the lag as well). The 100 hPa correlations between ΔT and Δq, as well as Δq and QBOI, increases to R = 0.81 and R = 0.80,

Figure 5. Interannual variability of the equatorial mean (180°E–180°W,08°S–08°N) of (a) temperature (ΔT), (b) water vapor (Δq), and (c) RH (ΔRH), in units of T, percent, and percent, respectively. (d) The Ocean Niño Index (ONI, red) and the quasi-biennial oscillation U50 index (QBOI, black). Green markers indicate ENSO events (see sections 2.2 and 2.3 for explanation of indices).

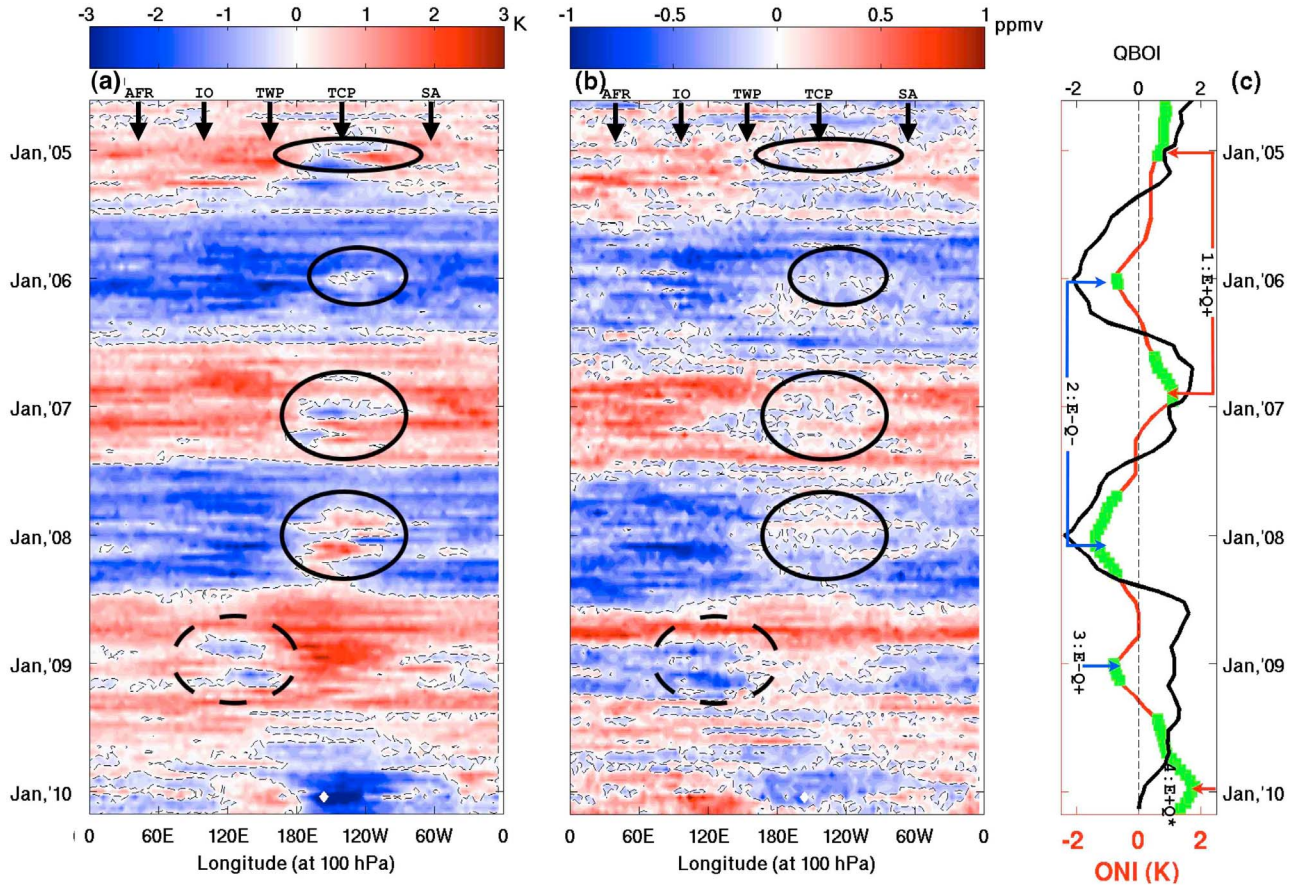

Figure 7. Longitude Hovmöller plots of (a) ΔT and (b) Δq, meridionally averaged in the 8°S–8°N band, at 100 hPa (longitude bins are 4°). (c) ONI and QBO are plotted for reference. The TWP and TCP are also marked out by arrows. Ovals mark breaks in the zonal symmetry of the QBO (dashed oval for the TWP). Figure 2 is inserted in Figure 7c for reference.

respectively, when excluding data beyond January 2008, which corresponds to when the ENSO and QBO begin to fall out of phase. This indicates possible different zonal impacts on water vapor depending on the relative phase of the ENSO and QBO. We note that doing correlations with time bins of ~16 days, on the one hand, yields more statistically significant time means, however, the coarseness of the time resolution prevents any probing of processes on scales finer than about a month. Thus, these lag correlations should only be seen as gross indications of relationships between remotely sensed parameters. Nevertheless, these correlations are statistically significant and confirm the strong influence of the QBO on the zonal temperature and water vapor structure, especially when the ENSO and QBO are in phase.

[34] Therefore, the zonal mean structure of tropopause temperature and water vapor primarily follow the QBO. However, this mean structure masks out the zonally varying ENSO signal seen, for example, by *Randel et al.* [2000] and *Gettelman et al.* [2001]. The ENSO and QBO are approximately in phase from August 2004 through boreal summer of 2008 (see Figure 3). After boreal summer of 2008 the ENSO and QBO fall out of phase. Some interesting questions to ask are: (1) how does 100 hPa ΔT depend on the phase of both interannual modes and (2) how is the water vapor distribution in the UTLS related to the relative phase of the ENSO and QBO. These questions will be addressed in more detail in sections 3.4.2–3.4.5.

3.4.2. Zonal Structure of the ENSO and QBO at 100 hPa

[35] In section 3.4.1 the equatorial mean time record was computed (8°S–8°N, 180°W–180°E). It was found that the QBO dominates the equatorial zonal mean ΔT and Δq structure at 100 hPa. However, since the time record in Figures 5 and 6 are tropical means, it is difficult to identify any ENSO signature at 100 hPa. Thus, the longitudinal variations are investigated to explore the regional impacts of the ENSO and QBO in the tropopause region.

[36] Figures 7a and 7b show longitude Hovmöller diagrams (8°S–8°N) of ΔT and Δq, respectively, at 100 hPa. The 100 hPa ΔT (Figure 7a) varies coherently with the phase of the QBOI indicating the dominating impact of the QBO on 100 hPa temperatures. However, upon closer inspection of 1:E+Q+ and 2:E−Q− (periods when the QBO and ENSO are approximately in phase) some interesting features are observed. The TWP anomalies have the same sign as the coherent QBO ΔT and exhibits warmer (colder) anomalies than other longitudes during El Niño (La Niña) events. This is consistent with larger (smaller) dehydration volumes occurring during La Niña (El Niño) seasons [*Zhou et al.*, 2004]. However, in the TCP, strands of opposite signed anomalies

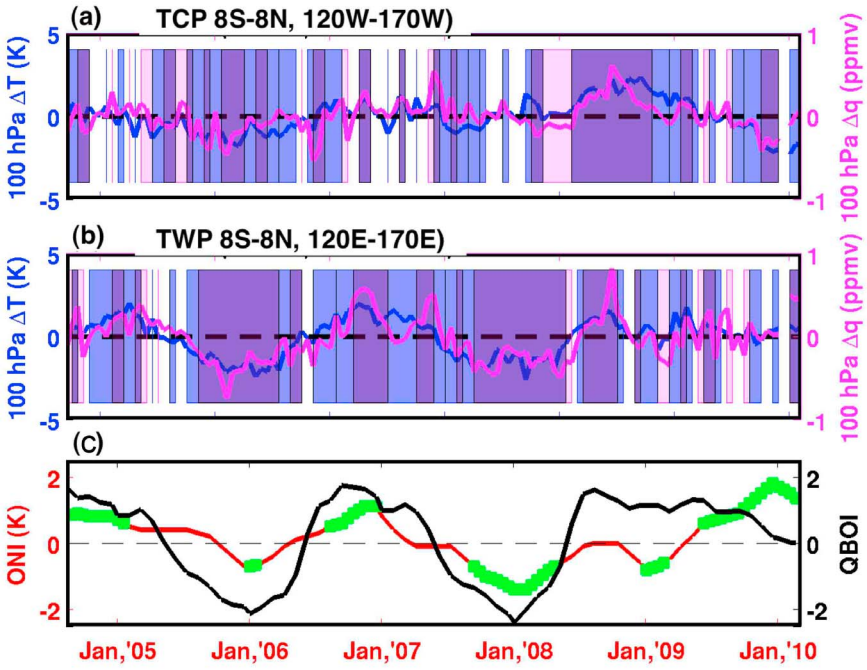

Figure 8. The 100 hPa ΔT (blue curve) and Δq (pink curve) for (a) TCP and (b) TWP. Blue patches correspond to time periods when ΔT signals are statistically significant at the 95% level or better. Pink patches quantify the same statistics for Δq. Periods with purple patches correspond to instances when ΔT and Δq are simultaneously statistically significant at the 95% level or better. (c) The ONI and QBOI are shown for reference.

exist. ENSO events that produce anomalies opposite to the prevailing QBO signal are circled with a solid black oval.

[37] From the boreal summer of 2008 to the first quarter of 2010 the ONI and QBOI are out of phase. The oscillating QBO signal produces a prevailing warm ΔT, especially between the boreal summers of 2008 and 2009 (composite 3:E−Q+). The ENSO and QBO temperature signatures are in phase in the TCP and the TWP experiences 100 hPa anomalies that are counter to the prevailing QBO signal. This is seen in the small blue bands circled with a dashed black oval. Figure 7b shows the strong impact of the QBO on the zonal 100 hPa Δq distribution. Colocated with the regional temperatures circled in Figure 7a are areas of positive (negative) Δq that correspond to positive (negative) ΔT. However, the spatial coherence is weaker than with ΔT.

[38] To statistically quantify the zonal breaks in ΔT and Δq at 100 hPa, the time record for the TCP (Figure 8a) and TWP (Figure 8b) are computed. Blue and pink patches indicate when ΔT and Δq, respectively, are statistically significant from 0 at the 95% confidence level; purple patches indicate when both anomalies are statistically significant.

[39] The 100 hPa ΔT in the TWP (blue curve in Figure 8b) show relatively large amplitudes during the years when the ONI and QBOI (shown in Figure 8c) are in phase, with ΔT that range between −2.6 to +2.0 K (between the end of 2004 to the boreal summer of 2008), with statistical significant at the 95% level much of this period. Δq is also statistically significant from 0 with anomalies that range between ±0.8 ppmv. During this period, the TCP experiences weaker anomalies with ΔT and Δq that range between −1.8 to +1.3 K and ±0.5 ppmv, respectively, with many oscillations around 0. When the QBOI and ONI fall out of phase (after the boreal summer of 2008), the TWP ΔT and Δq falls off to smaller magnitudes between −0.8 to +1.8 K and ±0.4 ppmv with frequent oscillations around 0. The TCP now experiences statically significant anomalies (at the 95% level), for longer periods of time, with ΔT and Δq ranging between −2.3 to +2.5 K and −0.4 to 0.5 ppmv, respectively. The TWP Δq, as with the equatorial mean case, correlates well with ΔT giving R = 0.77 (for lag +1), while the TCP shows a lower correlation of R = 0.62 (0 lag). This is consistent with previous work identifying that Δq is a function of the TWP CPT [e.g., *Holton and Gettelman*, 2001].

3.4.3. The 100 hPa Composite Maps of ΔT and Δq

[40] To investigate further this apparent zonal break in the QBO signal, the structures of the 100 hPa ΔT (Figure 9a) and Δq (Figure 9b) are investigated for boreal winter (DJF) in the context of the composites presented in Figure 2: 1:E+Q+, 2:E−Q−, 3:E−Q+, and 4:E +Q* (see section 2.2 for composite details). For 1:E+Q+, the QBO induced, zonally symmetric, warm ΔT shows a break of reduced ΔT centered around 120°W–170°W (Figure 9, dashed circled region). This also occurs in 2:E−Q− with the positive ΔT induced by ENSO breaking the zonal symmetry of the negative QBO ΔT. In both cases the ENSO and QBO are in phase and the observed ΔT around the zonal break forms a symmetrical dumbbell shaped pattern in the TCP since the zonal break has a maximum centered around 140W. These zonal asymmetries can also be interpreted as the QBO restricting (during the westerly regime, 1:E+Q+) or enhancing (during the easterly regime, 2:E−Q−) convection in the TWP [*Collimore et al.*, 1998, 2002].

[41] Transitioning to periods when the ENSO and QBO are out of phase, 3:E−Q+ shows a break in zonal ΔT that now

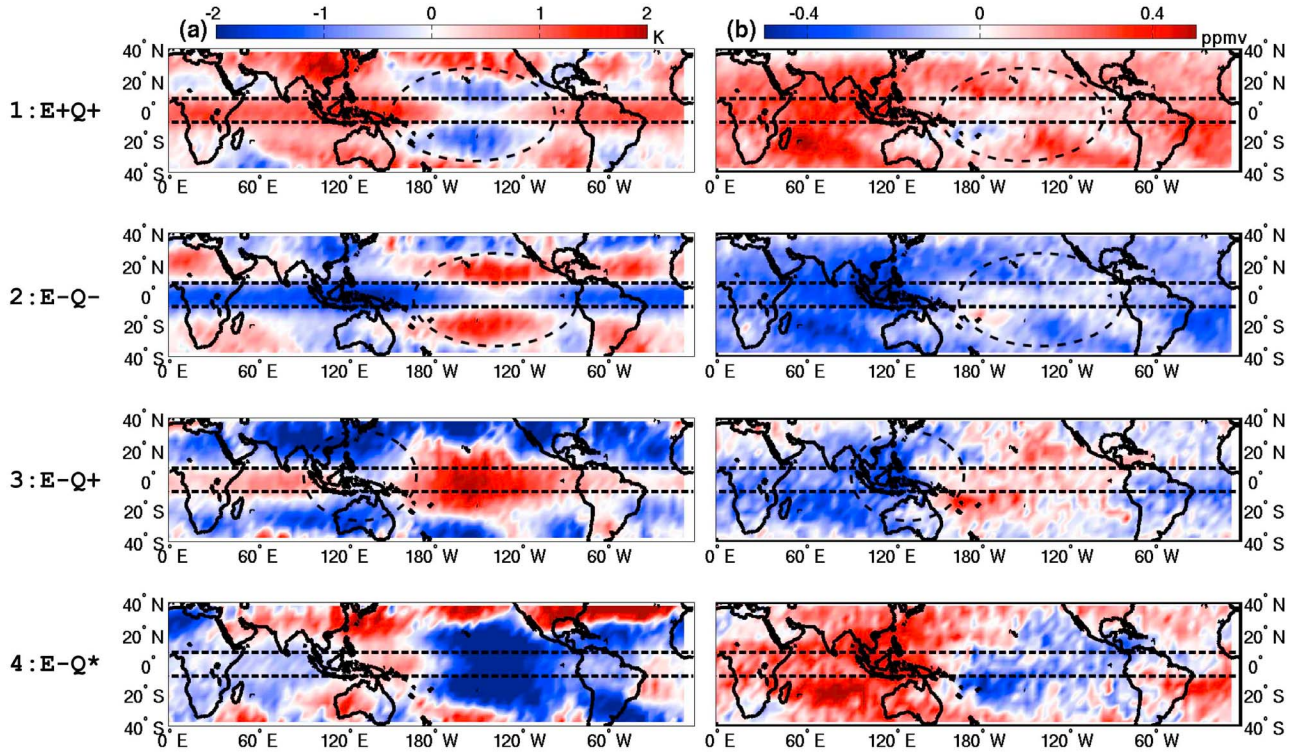

Figure 9. The 4° × 4° maps of 100 hPa (a) ΔT and (b) Δq for composite events 1:E+Q+ (first row), 2:E−Q− (second row), 3:E−Q+ (third row), and 4:E+Q* (fourth row) discussed in section 2.2. The star after Q indicates a nearly 0 QBOI. Dashed lines mark the 8°CS-8°CN band and the approximate meridional extent of the QBO signal in temperature.

occurs over the TWP (Figure 9, dashed circled region) with the TCP taking on zonal anomalies of the same sign as the prevailing westerly phase of the QBO. During this period the La Niña in itself should increase the dehydration potential of the TWP [e.g., *Zhou et al.*, 2004] via enhanced convection; however, the QBO westerly phase induces subsidence in the tropopause region, increasing tropopause temperatures, thus inhibiting convection from penetrating deeper into the tropopause region [*Collimore et al.*, 1998, 2002].

[42] The 4:E+Q* ΔT pattern appears, in contrast to the other ENSO events previously discussed, because the QBO is transitioning from the westerly to easterly phase, which takes place around boreal spring (see QBOI in Figure 2). Thus, the 4:E+Q* ΔT map shows the approximate temperature patterns one would expect with little influence from the QBO. The 4:E+Q* ΔT exhibits temperature patterns qualitatively consistent with the ENSO temperature patterns shown in Figure 6b of *Kiladis et al.* [2001]. The narrow band of warm anomalies in the TWP are enveloped by symmetrical cold anomalies around the equator in the TCP. These tropopause patterns are consistent with Rossby and Kelvin circulations induced by tropical equatorial heating [e.g., *Gill*, 1980; *Highwood and Hoskins*, 1998]. Figure 10 shows, in contrast to 4:E+Q*, a 3 month mean (August, September, October) in 2008 when the ONI is near zero and the QBO reaches a local maximum. The zonal symmetry in ΔT is robust in the tropics with very little evidence of an ENSO signature on tropopause temperatures. The weaker convection during the fall season and weak ENSO allow the QBO signal to manifest as a zonally symmetric feature in temperature and water vapor. Conceptually, the final signal in ΔT resembles a superposition of the QBO signal shown in Figure 10 and the ENSO signal in 4:E+Q* (Figure 9, fourth row).

[43] The Δq signals of 1:E+Q+ and 2:E−Q− show dominant prevailing signals that are in phase with the ONI and QBOI with 1:E+Q+ and 2:E−Q− showing positive and neg-

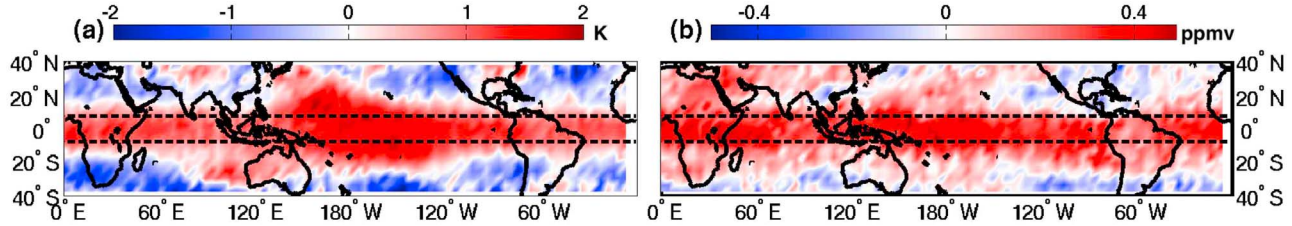

Figure 10. Same as Figure 9 but for a composite from the months of August–October (2008) when the ONI is nearly zero (see Figure 2).

ative water vapor anomalies, respectively. This is a consequence of the ENSO and QBO being in phase such that the zonally asymmetric ENSO feature does not show up strongly. Although the ENSO is responsible for the anomaly reduction in the TCP, the anomaly enhancement in the TWP dominates the zonal Δq distribution, consistent with Figures 6 and 8. However, 3:E−Q+ and 4:E+Q* both show the TCP with anomalies of the opposite sign from the rest of the tropics. In these cases, Δq is similar to ΔT in that a colder (warmer) tropopause corresponds to a drier (wetter) tropopause. This contrast in zonal Δq for 3:E−Q+ and 4:E+Q* suggests that when the ENSO and QBO are out of phase, the TCP may play a more prominent role in regulating the tropopause region water vapor distribution, though the source/sink of this water vapor cannot be determined from the composites.

[44] The resulting patterns of 100 hPa ΔT are interesting and have a simple explanation. During La Niña years (composite 2:E−Q− in Figure 9), deep convection is particularly strong in the TWP. This is associated with large positive temperature anomalies in the free troposphere due to convective heating (see Figure 3a). Associated with this strong heating is a thinner layer of anomalously cold temperatures around the tropopause region. In the TCP a warmer tropopause region is associated with colder free tropospheric temperatures. If the ENSO and QBO are in phase, then the cold ENSO anomalies will be in phase with the zonally symmetric cold QBO anomalies in the TWP, leading to an enhancement of cold anomalies, thus leading to greater dehydration in water vapor [*Zhou et al.*, 2004]. These same cold anomalies will work against the warm anomalies that are seen in the TCP tropopause temperatures, resulting in reduced anomalies. During the El Niño years that are in phase with the QBO (composite 1:E+Q+ in Figure 9), one expects the TCP to have colder tropopause temperatures. If the ENSO and QBO are in phase, once again, the zonally symmetric QBO signal, now positive (warm), will counteract the cold TCP tropopause temperatures while enhancing the warm tropopause temperatures in the TWP, leading to moistening/reduced dehydration in the TWP [*Zhou et al.*, 2004]. In these cases, the zonal structure of water vapor is primarily driven by the TWP CPT [*Holton and Gettelman*, 2001].

[45] During the periods when the ENSO and QBO are out of phase (3:E−Q+ and 4:E+Q* in Figure 9), the westerly (easterly) anomalies will enhance the TCP warm (cold) tropopause anomalies associated with La Niña (El Niño) events, while reducing the cold (warm) anomalies in the TWP. Revisiting 3:E−Q+, we find that a prominent water vapor maximum in TCP that is not present when the ENSO and QBO are in phase. This maximum is consistent with the La Niña warm top over the TCP being in phase with the warm QBO westerly, although the source of the water vapor maximum is not known.

3.4.4. Isolating the ENSO Signature

[46] In section 3.4.2, it was found that the ENSO and QBO either enhance or reduce temperature and water vapor anomalies at 100 hPa depending on the phase and location of observation. The anomalies are magnified in the TWP when the ENSO and QBO are in phase, leading to reduced anomalies in the TCP. When the ENSO and QBO are out of phase, the TCP becomes the region of enhanced anomalies while the TWP anomalies counter the prevailing QBO signal. Although the statistics seem to support this hypothesis, the ENSO effect still has not been quantified. In order to isolate the ENSO signal, the approximate zonal symmetry nature of the QBO is exploited. This is done by subtracting the tropical zonal mean time record (Figure 5) from the corresponding TCP and TWP time record.

[47] In the TWP, the correlation between ΔT_E and Δq_E (ΔT and Δq with their zonal mean subtracted out) at 100 hPa only yields R = 0.48. This is in contrast to the high correlation (R = 0.77, lag +1) for the case when the zonal mean is included. Within the TCP, the 100 hPa correlation between ΔT_E and Δq_E yields R = 0.82 (lag 0). This high value suggests that the local temperatures in the TCP do have a strong influence on the local water vapor distribution. During El Niño (La Niña) years, the TCP tropopause region cools (warms) leading to a dryer (moister) tropopause region. Recall, a weaker correlation was computed between ΔT and Δq with the zonal mean included (R = 0.62, lag 0). This, in part, may explain why when the ENSO and QBO are out of phase the TCP water vapor maxima shows up (e.g., 3:E−Q+). When the QBO and ENSO are out of phase, the ENSO impact on tropopause ΔT and Δq is now supported by the QBO.

3.4.5. Horizontal and Vertical Structure of the ENSO and QBO

[48] We now investigate the vertical and horizontal spatial distribution (Figure 11) of the interannual variability of temperature and water vapor to corroborate the results shown in sections 3.4.2–3.4.4. The same time period composites as shown in Figure 9 are selected for analyses, however, in order to highlight the impacts of ENSO, specifically El Niño, we compute the difference [1:E+Q+] − [2:E−Q−] (herein EL01, brackets inserted for readability) and [4:E+Q*] − [3:E−Q+] (herein EL02).

[49] The EL01 ΔT composite (Figure 11a) shows a strong thick band of warm QBO anomalies from 50 hPa down into the TTL. The TWP TTL shows especially warm anomalies as compared to the rest of the tropics contrasting the thin vertical band of cold anomalies over the TCP TTL. The tropical troposphere is also warm. As previously discussed (section 3.4.2), the ENSO dominates the free tropospheric and boundary layer zonal mean ΔT. Subtracting the zonal mean ΔT produces ΔT_E (Figure 11c), revealing the asymmetrical ENSO anomalies (with possible other effects as well, for example, tropospheric biennial oscillations which impacts aspects of the rainfall associated with the Indian Monsoon [*Chang and Li*, 2000]). A quadrupole temperature anomaly structure is revealed in ΔT_E, with a cold top over a warm free troposphere in the TCP and colder free troposphere in the TWP with a warm top. A quadrupole pattern in Δq_E is roughly colocated with the ΔT_E structure. However, there are a few differences in the water vapor structure. First, the tropospheric anomalies in Δq_E extend into the bottom of the TTL where one finds ΔT_E with opposite sign to Δq_E. Secondly, the layer of TTL Δq_E anomalies primarily lie above 100 hPa in the TCP, whereas ΔT_E is approximately symmetric around 100 hPa. Thus, although the ENSO impacts on temperature are symmetric around the tropopause, its impact on water vapor is skewed into the stratospheric region.

[50] The ΔT_E signal for EL01 clearly shows the cold TCP TTL is playing a role in reducing the warm QBO anomalies while the warm TWP TTL (Figure 11c) enhances the QBO signal. Associated with these warm anomalies is hydra-

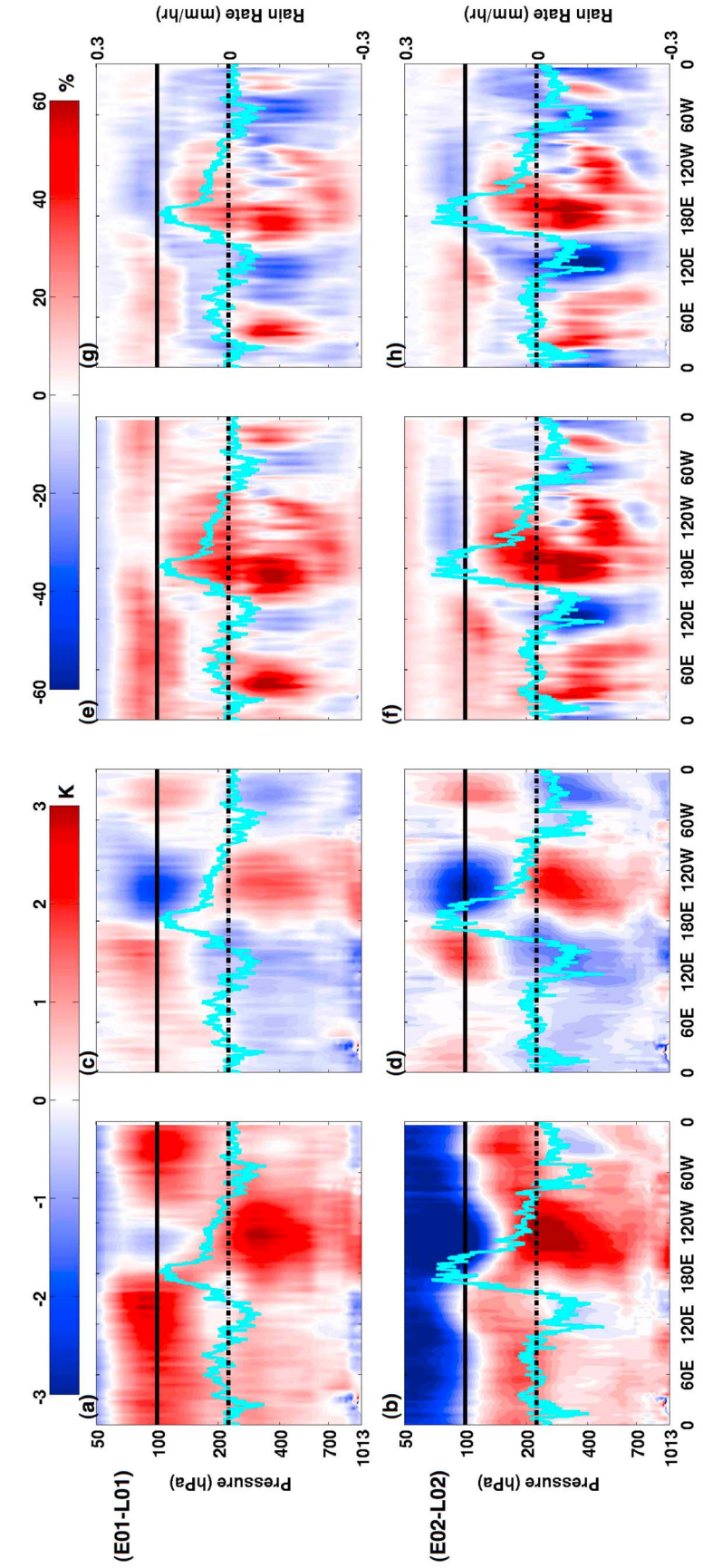

Figure 11. Vertical cross sections of: (a and b) ΔT, (c and d) ΔT with the zonal mean removed (ΔT_E), (e and f) Δq, and (g and h) Δq with the zonal mean removed (Δq_E) for composite differences between [1:E+Q+] − [2:E−Q−] (EL01, Figures 11a, 11c, 11e, and 11g) and [4:E+Q*] − [3:E−Q+] (EL02, Figures 11b, 11d, 11f, and 11h) (composite events shown in Figure 9). Ordinate is pressure in hPa and abscissa longitude (4° bins); meridional mean is taken from 8°S–8°N. Overlaid solid black horizontal line marks 100 hPa. Overlaid blue curve is the interannual mean rain rate anomalies (Δrr), in mm/h, derived from TRMM with ordinate axes on the right; dash-dotted line marks zero Δrr.

tion of the TTL region over the TWP (in a La Niña case, i.e., [2:E−Q−] − [1:E+Q+], there would be enhanced dehydration, highlighting composite 2:E−Q−). Upon further inspection, one finds that the mean Δq, i.e., the mean Δq difference [1:E+Q+] − [2:E−Q−], in the TCP is ~2 % (~0.1 ppmv), while the TWP mean is ~12 % (~0.4 ppmv). EL02 shows that deep convection in the TCP leads to cold TTL ΔT_E that enhances the QBO cold anomalies. The overlaid (light blue curves in Figure 11) interannual rain rate anomalies (Δrr, in mm/hr), computed from Tropical Rainfall Measuring Mission [*Iguchi et al.*, 2000] data corroborates that convection follows the ENSO cycle; high Δrr follows the tropospheric moistening. For EL02, the TCP cold anomalies associated with deep convection are now allowed to constructively work with the QBO to dehydrate TTL air over the TCP, or in the case of 3:E−Q+ (a La Niña), moisten the TTL TCP. In the case of [3:E−Q+] − [4:E+Q*] (highlighting La Niña), the mean TCP and TWP differences in Δq are ~+8 % (~+0.3 ppmv) and ~−13 % (~−0.4 ppmv), respectively, with the TCP TTL anomalies now switching signs. Although 3:E−Q+ shows a moist anomaly over the TCP, presumably from the QBO westerly anomaly and La Niña warm top having the same sign, the source of this water vapor cannot be determined from this analysis.

4. Discussion and Conclusions

[51] We have utilized a merged temperature (AIRS) and water vapor (AIRS and MLS) data set [*Liang et al.*, 2010] to create a full-atmospheric time record of temperature and water vapor quantifying both the annual cycle and interannual variability of these quantities. This data set captures, in a self-consistent way, the connection between the troposphere and stratosphere for temperature and water vapor, something that previous observation records could not capture, especially for water vapor. From the seasonal and annual cycle, we estimated the mean water vapor concentrations, q_s, and temperature as a function of various locations. Our estimates, within instrument uncertainty, are consistent with previous estimates of these values and indicate that the AIRS and MLS combined data set does capture the zonal structure of the tropics well.

[52] We were also able to identify the interannual signals of the ENSO and QBO, showing that the boundary layer and free tropospheric interannual variations of convection can cancel or enhance tropopause region temperature anomalies depending on the location and phase of the ENSO and QBO. When the ENSO and QBO are in phase the TWP temperature anomalies are enhanced while the TCP experiences anomalies counter the prevailing QBO anomalies. However, when these interannual modes are out of phase, the TCP experiences the anomaly enhancements with the TWP showing weaker anomalies. The hypothesis that these anomaly enhancements and cancellations are a result of changes to the Walker Circulation, which lead to a migration of convection between the TCP and TWP, is further supported by the migration of free tropospheric water vapor anomalies and the local strengthening or weakening of regional rain rates. However, we found that when the ENSO and QBO are in phase the ENSO impact on the zonal water vapor distribution is masked by the QBO, though we do identify enhanced (weakened) dehydration in the TWP and zonal mean water vapor, consistent with previous work [*Zhou et al.*, 2004]. On the other hand, when the ENSO and QBO are not in phase, the ENSO impact on water vapor is not only highlighted in the TWP but also the TCP. This is consistent with the enhanced warming observed in 3:E−Q+ over the TCP. In addition, the high correlation between ΔT_E and Δq_E suggests that water vapor in the TCP is locally regulated. However, more work needs to be done to investigate water vapor transport processes in the TCP, particularly when the ENSO and QBO are out of phase. We note that our results particularly apply to boreal winter interactions of the ENSO and QBO. *Zhou et al.* [2004] indicated that not only does the relative phase of the ENSO and QBO matter but also the time of year they interact. However, they do indicate that the interaction between the ENSO and QBO are at a maximum during boreal winter since tropical convection and tropopause height are also at a maximum during this time of year. Our findings are consistent with their results.

[53] Figure 11 also highlights that while there are quadrupole patterns of anomalies in temperature (ΔT_E) and water vapor (Δq_E), the spatial extent of the anomalies are different. In temperature, the anomalies due to convection in the troposphere only reach ~200 hPa, roughly the location of neutral buoyancy in the tropics, however, the water vapor anomalies reach ~120 hPa. In the TTL, the temperature anomalies are roughly symmetric about the tropopause but water vapor shows particularly strong anomalies in the LS especially over the TCP. Because our calculations only capture an Eulerian framework of the temperature and water vapor distribution, it is difficult to determine the possible transport pathways that determine the regional water vapor structure. For example, although 3:E−Q+ shows enhanced warming and moistening over the TCP, the source of this moistening cannot be determined from our analysis. Although, since 3:E−Q+ was during a La Niña, convective injection from the TCP is not likely the source of the observed stratospheric moist anomaly. A longer time series would aid in corroborating our findings. It is also important to note that we cannot, from the observations, determine whether the zonal asymmetries are a linear superposition of the ENSO and QBO impact on the tropopause or a coupling between the two interannual modes. There is evidence, however, that the ENSO can alter planetary waves and their propagation that may modulate the magnitude and phase of the QBO [*Dunkerton*, 1997].

[54] What has not been addressed in this work is the role of clouds in the TTL. It is well known that the TWP has a high frequency of occurrence of thin cirrus [e.g., *Comstock et al.*, 2004] and is frequently supersaturated (see Table 1). *Holton and Gettelman* [2001] showed in their simulations that the TWP could in principle dehydrate air to the water vapor concentrations consistent with lower stratospheric values from frequent horizontal passes of air parcels through this cold region heavily populated by TTL cirrus. Furthermore, the presence of TTL cirrus modulates the level of zero radiative heating (LZRH), a metric of the radiative balance in the tropical atmosphere [*Gettelman et al.*, 2004; *Corti et al.*, 2005]. The radiative balance determines the location where tropical upwelling departs from being primarily convective to becoming radiatively driven. Thus, the tropical distribution of TTL cirrus is important for not only quantifying the water vapor distribution but also the time scale of its transport.

[55] Our findings do have some implications. From a regional atmospheric process perspective, we found that the TCP can play a significant role in impacting the zonal water vapor distribution, particularly when the ENSO and QBO are out of phase. Since it is still not known if there is a preferred tropical longitude for where water vapor enters the stratosphere [e.g., *Dessler*, 1998], the TCP, in principle, can impact the stratospheric water vapor tape recorder. The presence of the 3:E−Q+ moist anomaly over the TCP stratosphere is evidence of this impact. From a modeling standpoint, any model would need to capture the relative phase of the ENSO and QBO correctly, to simulate the interannual impacts on the zonal water vapor distribution correctly. Furthermore, if high cloud amount is found to be crucial in quantifying UTLS water vapor, models would need to capture the correct horizontal and vertical distribution of clouds.

[56] **Acknowledgments.** C. K. Liang would like to thank H. Nguyen for helpful discussion on determining statistical significance for remote sensing time series records. The authors would also like to thank W. J. Randel for helpful discussion on aspects of the QBO. C. K. Liang was supported by a NASA Earth and Space Science Fellowship (NNX09AO04H) and Northrop Grumman fellowship. AIRS and MLS data were obtained through the Goddard Earth Sciences Data and Information Services Center (http://daac.gsfc.nasa.gov/). This work was performed at the Jet Propulsion Laboratory, California Institute of Technology.

References

Andrews, D. G., J. R. Holton, and C. B. Leovy (1987), *Middle Atmosphere Dynamics*, *Int. Geophys. Ser.*, vol. 40. Academic, San Diego, Calif.

Aumann, H. H., et al. (2003), AIRS/AMSU/HSB on the Aqua mission: Design, science objectives, data products, and processing systems *IEEE Trans. Geosci. Remote Sens.*, *41*, 253–264.

Baldwin, M. P., et al. (2001), The Quasi-Biennial Oscillation, *Rev. Geophys.*, *39*, 179–229.

Brewer, A. M. (1949), Evidence for a world circulation provided by the measurements of helium and water vapor distribution in the stratosphere, *Q. J. R. Meteorol. Soc.*, *75*, 351–363.

Chahine, M. T., T. S. Pagano, and H. H. Aumann (2006), The Atmospheric Infrared Sounder (AIRS): Improving weather forecasting and providing new insights into climate, *Bull. Am. Meteorol. Soc.*, *87*, 911–926, doi:10.1175/BAMS-87-7-911.

Chang, C. P., and T. Li (2000), A theory for the Tropical Tropospheric Biennial Oscillation, *J. Atmos. Sci.*, *57*, 2209–2224.

Collimore, C. C., M. H. Hitchman, and D. W. Martin (1998), Is there a quasi-biennial oscillation in tropical convection?, *Geophys. Res. Lett.*, *25*, 333–336.

Collimore, C. C., D. W. Martin, M. H. Hitchman, A. Huesmann, and D. Waliser (2002), On the relationship between the QBO and tropical deep convection, *J. Clim.*, *16*, 2552–2568.

Comstock, J., T. Ackerman, and D. Turner (2004), Evidence of high ice supersaturation in cirrus clouds using ARM Raman lidar measurements, *Geophys. Res. Lett.*, *31*, L11106, doi:10.1029/2004GL019705.

Corti, T., B. P. Luo, P. Peter, H. Vömel, and Q. Fu (2005), Mean radiative energy balance and vertical mass fluxes in the equatorial upper troposphere and lower stratosphere, *Geophys. Res. Lett.*, *32*, L06802, doi:10.1029/2004GL021889.

Dessler, A. E. (1998), A reexamination of the "stratospheric fountain" hypothesis, *Geophys. Res. Lett.*, *25*, 4165–4168.

Divakarla, M. G., C. D. Barnet, M. D. Goldberg, L. M. McMillin, E. Maddy, W. Wolf, L. Zhou, and X. Liu (2006), Validation of Atmospheric Infrared Sounder temperature and water vapor retrievals with matched radiosonde measurements and forecasts, *J. Geophys. Res.*, *111*, D09S15, doi:10.1029/2005JD006116.

Dunkerton, T. (1985), A two-dimensional model of the quasi-biennial oscillation, *J. Atmos. Sci.*, *42*, 1151–1160.

Dunkerton, T. (1997), The role of gravity waves in the quasi-biennial oscillation, *J. Geophys. Res.*, *102*, 26,053–26,076.

Fetzer, E. J., et al. (2008), Comparison of upper tropospheric water vapor observations from the Microwave Limb Sounder and Atmospheric Infrared Sounder, *J. Geophys. Res.*, *113*, D22110, doi:10.1029/2008JD010000.

Fueglistaler, S., and P. H. Haynes (2005), Control of interannual longer-term variability of stratospheric water vapor, *J. Geophys. Res.*, *110*, D24108, doi:10.1029/2005JD006019.

Fueglistaler, S., M. Bonazzola, P. H. Haynes, and T. Peter (2005), Stratospheric water vapor predicted from the Lagrangian temperature history of air entering the stratosphere in the tropics, *J. Geophys. Res.*, *110*, D08107, doi:10.1029/2004JD005516.

Fueglistaler, S., A. E. Dessler, S. Dunkerton, I. Folkins, Q. Fu, and P. W. Mote (2009), Tropical tropopause layer, *Rev. Geophys.*, *47*, RG1004, doi:10.1029/2008RG000267.

Geller, M. A., Z. Zhou, and M. Zhang (2002), Simulations of interannual variability of stratospheric water vapor, *J. Atmos. Sci.*, *59*, 1076–1085.

Gettelman, A., and Q. Fu (2008), Observed and simulated upper-tropospheric water vapor feedback, *J. Clim.*, *21*, 3282–3289, doi:10.1175/2007JCLI2142.1.

Gettelman, A., W. J. Randel, S. T. Massie, F. Wu, W. Read, and J. Russell (2001), El Niño as a natural experiment for studying the tropical tropopause region, *J. Clim.*, *14*, 3375–3392.

Gettelman, A., P. M. D. F. Forster, F. Masatomo, Q. Fu, H. Vömel, L. K. Gohar, C. Johanson, and M. Ammerman (2004), Radiation balance of the tropical tropopause layer, *J. Geophys. Res.*, *109*, D07103, doi:10.1029/2003JD004190.

Gill, A. E. (1980), Some simple solutions for heat-induced tropical circulations, *Q. J. R. Meteorol. Soc.*, *106*, 447–462.

Hamilton, K. (1984), Mean wind evolution through the quasi-biennial cycle in the tropical lower stratosphere, *J. Atmos. Sci.*, *41*, 2113–2125.

Held, I. M., and B. J. Soden (2000), Water vapor feedback and global warming, *Annu. Rev. Energy. Environ.*, *25*, 441–475.

Highwood, E. J., and B. J. Hoskins (1998), The tropical tropopause, *Q. J. R. Meteorol. Soc.*, *124*, 1579–1604.

Holloway, C. E., and J. D. Neelin (2007), The convective cold top and quasi equilibrium, *J. Atmos. Sci.*, *64*, 1467–1487.

Holton, J. R., and A. Gettelman (2001), Horizontal transport and the dehydration of the stratosphere, *Geophys. Res. Lett.*, *28*, 2799–2802.

Horváth, A., and B. J. Soden (2007), Lagrangian diagnostics of tropical deep convection and its effect upon upper-tropospheric humidity, *J. Clim.*, *21*, 1013–1028.

Huesman, A. S., and M. H. Hitchman (2001), The stratospheric quasi-biennial oscillation in the NCEP reanalyses: Climatological structures, *J. Geophys. Res.*, *106*, 11,859–11,874.

Iguchi, T., T. Kozu, R. Meneghini, J. Awaka, and K. Okamoto (2000), Rain-profiling algorithm for the TRMM precipitation radar, *J. Appl. Meteorol.*, *39*, 2038–2052.

Kiladis, G. N., H. K. Straub, G. C. Reid, and K. S. Gage (2001), Aspects of interannual and intraseasonal variability of the tropopause and lower stratosphere, *Q. J. R. Meteorol. Soc.*, *127*, 1961–1983.

Kirk-Davidoff, D. B., E. J. Hintsa, J. G. Anderson, and D. W. Keith (1999), The effect of climate change on ozone depletion through changes in stratospheric water vapour, *Nature*, *402*, 399–401.

Liang, C. K., A. Eldering, F. W. Irion, W. G. Read, E. J. Fetzer, B. H. Kahn, and K.-N. Liou (2010), Characterization of merged AIRS and MLS water vapor sensitivity through integration of averaging kernels and retrievals, *Atmos. Meas. Tech. Discuss.*, *3*, 2833–2859, doi:10.5194/amtd-3-2833-2010.

Mitchell, T. P., and J. M. Wallace (1992), The annual cycle in equatorial convection and sea-surface temperature, *J. Clim.*, *5*, 1140–1156.

Mote, P. W., K. H. Rosenlof, J. R. Holton, R. S. Harwood, and J. W. Waters (1996), An atmospheric tape recorder: The imprint of tropical tropopause temperatures on stratospheric water vapor, *J. Geophys. Res.*, *101*, 8651–8666.

Murphy, D. M., and T. Koop (2005), Review of the vapour pressures of ice and supercooled water for atmospheric applications, *Q. J. R. Meteorol. Soc.*, *131*, 1539–1565.

Philander, S. G. (1990), *El Niño, La Niña, and the Southern Oscillation*, *Int. Geophys. Ser.*, vol. 46. Academic, San Diego, Calif.

Randel, W. J., F. Wu, J. M. Russel III, A. Roche, and J. Waters (1998), Seasonal cycles and QBO variations in stratospheric CH_4 and water vapor observed in UARS HALOE data, *J. Atmos. Sci.*, *55*, 163–185.

Randel, W. J., F. Wu, and D. J. Gaffen (2000), Interannual variability of the tropical tropopause derived from radiosonde data and NCEP reanalyses, *J. Geophys. Res.*, *105*, 15,509–15,523.

Read, W. G., et al. (2007), Aura Microwave Limb Sounder upper tropospheric and lower stratospheric H_2O and relative humidity with respect to ice validation, *J. Geophys. Res.*, *112*, D24S35, doi:10.1029/2007JD008752.

Reed, R. J. (1965a), The present status of the 26-month oscillation, *Bull. Am. Meteorol. Soc.*, *46*, 374–387.

Reed, R. J. (1965b), The quasi-biennial oscillation of the atmosphere between 30 and 50 km over Ascension Island, *J. Atmos. Sci.*, *22*, 331–333.

Russell, J. M., III, A. F. Tuck, L. L. Gordley, J. H. Park, S. R. Drayson, J. E. Harries, R. J. Cicerone, and P. J. Crutzen (1993), The HALOGEN Occultation Experiment, *J. Geophys. Res.*, *98*, 10,777–10,797.

Santer, B., et al. (2005), Amplification of surface temperature trends and variability in the tropical atmosphere, *Science*, *309*, 1551, doi:10.1126/science.1114867.

Sherwood, S. C., and A. E. Dessler (2001), A model for transport across the tropical tropopause, *J. Atmos. Sci.*, *58*, 765–779.

Sherwood, S. C., and A. E. Dessler (2003), Convective mixing near the tropical tropopause: Insights from seasonal variations, *J. Atmos. Sci.*, *60*, 2674–2685.

Soden, B. J. (2004), The impact of tropical convection and cirrus on upper tropospheric humidity: A Lagrangian analysis of satellite measurements, *Geophys. Res. Lett.*, *31*, L20104, doi:10.1029/2004GL020980.

Soden, B. J., and F. P. Bretherton (1993), Upper-tropospheric relative humidity from the GOES 6.7 μm channel: Method and climatology for July 1987, *J. Geophys. Res.*, *98*, 16,669–16,688.

Soden, B. J., D. L. Jackson, V. Ramaswamy, M. Schwarzkopf, and X. Huang (2005), The radiative signature of upper tropospheric moistening, *Science*, *310*, 841–844.

Solomon, S., K. H. Rosenlof, R. W. Portmann, J. S. Daniel, S. M. Davis, T. J. Sanford, and G.-K. Plattner (2010), Contributions of stratospheric water vapor to decadal changes in the rate of global warming, *Science*, *327*, 1219–1223.

Susskind, J., C. D. Barnet, J. Blaisdell, L. Iredell, F. Keita, L. Kouvaris, G. Molnar, and M. Chahine (2006), Accuracy of geophysical parameters derived from Atmospheric Infrared Sounder/Advanced Microwave Sounding Unit as a function of fractional cloud cover, *J. Geophys. Res.*, *111*, D09S17, doi:10.1029/2005JD006272.

Tobin, D. C., H. E. Revercomb, R. O. Knuteson, B. M. Lesht, L. L. Strow, S. E. Hannon, W. F. Feltz, L. A. Moy, E. J. Fetzer, and T. S. Cress (2006), Atmospheric Radiation Measurement site atmospheric state best estimates for AIRS temperature and water vapor retrieval validation, *J. Geophys. Res.*, *111*, D09S14, doi:10.1029/2005JD006103.

Wallace, J. M. (1973), General circulations of the tropical lower stratosphere, *Rev. Geophys.*, *11*, 191–222.

Wallace, J. M., E. M. Rasmusson, T. P. Mitchell, V. E. Kousky, E. S. Sarachik, and H. von Storch (1998), The structure and evolution of ENSO-related climate variability in the tropical Pacific: Lessons from TOGA, *J. Geophys. Res.*, *103*, 14,241–14,251.

Waters, J. W., et al. (1999), The UARS and EOS Microwave Limb Sounder experiments, *J. Atmos. Sci.*, *56*, 194–218.

Waters, J. W., L. Froidevaux, R. S. Harwood, and R. F. Jarnot (2006), The Earth Observing System Microwave Limb Sounder (EOS MLS) on the Aura satellite, *IEEE Trans. Geosci. Remote Sens.*, *44*, 1075–1092.

Zhou, X. L., M. A. Geller, and M. H. Zhang (2001a), Cooling trends of the tropical cold point tropopause temperatures and its implications, *J. Geophys. Res.*, *106*, 1511–1522.

Zhou, X. L., M. A. Geller, and M. H. Zhang (2001b), Tropical cold point tropopause characteristics derived from ECMWF reanalyses and soundings, *J. Clim.*, *14*, 1823–1838.

Zhou, X. L., M. A. Geller, and M. H. Zhang (2004), Temperature fields in the tropical tropopause transition layer, *J. Clim.*, *17*, 2901–2908.

A. Eldering, E. J. Fetzer, B. Tian, and S. Wong, Jet Propulsion Laboratory, California Institute of Technology, Pasadena, CA 91109, USA. (annmarie.eldering@jpl.nasa.gov; eric.j.fetzer@jpl.nasa.gov; baijun.tian@jpl.nasa.gov; sun.wong@jpl.nasa.gov)

A. Gettelman, Atmospheric Chemistry Division, National Center for Atmospheric Research, Boulder, CO 80307-3000, USA. (andrew@ucar.edu)

C. K. Liang and K. N. Liou, Joint Institute for Regional Earth System Science and Engineering, University of California, Los Angeles, CA 90095, USA. (cliang@atmos.ucla.edu; knliou@atmos.ucla.edu)